Attributing impacts of LULCC on the boundary layer climate of South Africa's eastern escarpment

Tumelo Mohomi[1]*, Nkanyiso B. Mbatha[2], Danie S. Boshoff[1], Innocent L. Mbokodo[3], Thando Ndarana[4], Mary-Jane M. Bopape[5] and Hector Chikoore[6]

[1]Unit for Environmental Sciences and Management, North-West University, Vanderbijlpark 1900, South Africa; mohomitumelo@icloud.com and daniebshff@gmail.com
[2]Department of Geography and Environmental Studies, University of Zululand, KwaDlangezwa 3886, South Africa; MbathaNB@unizulu.ac.za
[3]Climate Service, South African Weather Service, Pretoria 0001, South Africa. innocent.mbokodo@weathersa.co.za
[4]Department of Geography, GeoInformatics and Meteorology, University of Pretoria, Hatfield 0028, South Africa; thando.ndarana@up.ac.za
[5]South African Environmental Observation Network, National Research Foundation, Pretoria 0083, South Africa; mm.bopape@saeon.nrf.ac.za
[6]Department of Geography and Environmental Studies, University of Limpopo, Sovenga 0727, South Africa; hector.chikoore@ul.ac.za

*Corresponding author email: mohomitumelo@icloud.com

Abstract

Land surface characteristics may influence the planetary boundary layer atmosphere and climate through exchanges of moisture, energy, and momentum near the surface. We attributed the impact of multitemporal landsat-derived land use/land cover change (LULCC) on temperature and precipitation variability in eastern South Africa using reanalysis data and satellite-derived estimates from 1979 to 2020. Landsat images were classified into different land cover classes using a machine learning random forest pixel-based supervised algorithm within the cloud-based Google Earth Engine. Time series analysis was employed to analyze cycles and trends in LULCC and hydrometeorological variables, whilst the variable importance model determined the most sensitive variable. The impacts of LULCC on the boundary layer climate were attributed via multiple linear regression. An uninterrupted rapid expansion of urban areas was observed, resulting in the transformation of grasslands, water bodies, forests, and croplands. Statistically significant changes in moisture and energy fluxes, and hydrometeorological variables were observed across the study period. Latent heat flux (LHF), as well as rainfall decreased, while

maximum temperature, sensible heat, and potential evapotranspiration (PET) increased significantly. We found that LULCC is significantly impacting the boundary layer climate, with urban and bare land, grasslands, forests, and croplands influencing temperature positively while negatively influencing rainfall. Rainfall was most sensitive to changes in LHF, whilst the key driver of temperature variability was PET. Our results reinforce the significance of LULCC and associated feedbacks to understanding boundary layer processes, climate variability, and change.

Keywords. LULCC; climate variability and change; variable importance; random forest; surface moisture and energy fluxes; planetary boundary layer.

1. Introduction

The land surface is among the planet's most valuable and scarce natural resources (Atayi *et al*. 2016), important for human population growth and providing mankind with access to basic survival necessities such as shelter, food (Musetsho *et al*. 2021), water, medications, and energy (Rounsevell *et al*. 2014). Whilst land use is the anthropogenic modification of land for urban settlement, agriculture, recreation, and grazing land (Briassoulis 2009; Atayi *et al*. 2016), land cover refers to the physical characteristics of the earth's surface such as vegetation, water, soil, and paved surfaces (Briassoulis 2009; Tizora *et al*. 2016). Global resource demand has increased pressure on land use and land cover (LULC) to meet the needs of the growing population and provide a better life (Garg *et al*. 2019; Herrmann *et al*. 2020; Musetsho *et al*. 2021). Population growth also accelerates urban and cropland expansion at the expense of other land cover types, such as grasslands (Dong *et al*. 2019). The land surface is being altered regularly due to infrastructure development especially in developing countries, with the aim to improve living conditions and boost economies. Thus, land use and land cover change (LULCC) exemplify the earth's response to human-induced pressures and has become a significant contributor to the changing global climate.

Climate change hastens the severity of natural processes and climate extremes such as droughts, heat waves, and floods (Solanky *et al*. 2018; Yuvaraj 2020), which also modify and transform the land surface. Climate extremes have become more frequent and more severe, increasing the

vulnerability of rural communities and ecosystems in developing countries. Although human activities are the primary cause of LULCC and the current climate change, natural processes also play a role (Liu *et al*. 2017; Herrmann *et al*. 2020; Musetsho *et al*. 2021). Several regions around the world have experienced increased climate variability as a result of LULCC (Dong *et al*. 2019), altering regional air circulation, surface energy, and moisture fluxes (Pontifes *et al*. 2018). Economic growth and urbanization have increased greenhouse gas concentrations, making them major contributors to global warming.

LULCC is often associated with changes in infiltration, evapotranspiration (ET), groundwater recharge, and surface run-off. Changes in land surface characteristics have significant impacts on energy and moisture exchanges between the earth's surface and the lower atmosphere (Li *et al*. 2020). These exchanges influence how latent and sensible heat fluxes are partitioned near the surface, which may impact the climate system (Ban-Weiss *et al*. 2011). Moisture in the soil and vegetation increases ET fluxes, which cools the surrounding environment by transferring more energy as latent heat. While in some regions, a densely vegetated area can receive twice as much precipitation compared to a sparsely vegetated area (Mahmood *et al*. 2014), changes in vegetation patterns can alter precipitation and contribute to climate change.

Africa, a biodiverse continent, is one of the world's fastest-urbanizing regions, experiencing uncontrolled and unplanned urbanization (Güneralp *et al*. 2018), which, according to Turok and Borel-Saladin (2014), degrades ecosystem quality and increases environmental risk and resource scarcity. These unplanned settlements are subjected to greater urban heat island (UHI) effects than planned settlements (Ngie 2020). The increased extent and significance of LULCC and its impact on climate has received increasing research attention in southern Africa. Several studies have investigated the relationship between LULCC and climate in a variety of ways (Li *et al*. 2011; Pielke *et al*. 2011; Oki and Blyth 2012; Li *et al*. 2018; Ge *et al*. 2019; Idowu *et al*. 2019; Huang *et al*. 2020; Meer and Mishra 2020).

Prior research has focused on the spatial distribution of LULCC (Odindi *et al*. 2012; Xulu 2014; Tizora *et al*. 2016; Kamwi *et al*. 2018; Phan *et al*. 2021), its influence on land surface temperature (LST) and UHI (Mbithi *et al*. 2006; Li *et al*. 2011; Ding and Shi 2013; Idowu *et al*. 2019;

Sanecharoen *et al*. 2019), precipitation (Meer and Mishra 2020; Thapa 2020) and air temperature (Xiaofang *et al.* 2017). Due to the activities of the construction and sand mining industry, Tizora *et al*. (2016) found a significant decrease in natural surfaces in South Africa's Western Cape Province and a dominant increase in mines and pits due to LULCC. Moreover, deforestation and residential development have resulted in 25.5% of Rustenburg city expansion and fragmentation of South Africa's essential biodiversity (Mudau *et al*. 2014; Musetsho *et al*. 2021) and are primary contributors to the impact on hydrology, water quality, and availability in South Africa (Gyamfi *et al*. 2016; Namugize *et al*. 2018; Nkosi *et al*. 2021). Urban sprawl has increased surface warming in several municipalities such as Ethekwini, Buffalo, and Nelson Mandela Bay including metropolitan cities of Durban, Johannesburg, and Cape Town (Odindi *et al.* 2015, 2017; Ngie *et al*. 2017; Magidi and Ahmed 2020; Ngie 2020). Overall, studies have demonstrated the widespread presence of LULCCs in South Africa, as well as their impact on ecosystem services and climate change. However, there is limited research that has attributed the impacts of LULCC to observed changes in the boundary layer climate.

Understanding the relationship and impact of LULCC on surface heat flux, moisture flux, and hydrometeorological variables is important, particularly in eastern South Africa. The area is a major maize-producing region dominated by savanna and grassland biomes, whilst intensive crop cultivation significantly fragments and degrades natural vegetation (Botha *et al*. 2015). Eastern South Africa is an excellent location for evaluating the impact of LULCC since the area receives higher rainfall and has more vegetation than the arid west (Landman *et al*. 2017). It is dominated by vegetation biomes such as grasslands and savannas and located over the eastern escarpment, critical in influencing the atmospheric circulation and acting as a barrier to airflow, often enhancing rainfall due to the uplift of moisture (Singleton and Reason 2006; Ogwang *et al*. 2014; Chikoore *et al*. 2021). It is critical to understand how land has been altered in eastern South Africa and the resultant impact on the local climate, as well as to determine which LULC class has the greatest influence on the change of the local boundary layer climate. This will aid in future disaster preparedness and policy formulation, as well as environmental protection, increased agricultural production, and human life preservation.

In view of the foregoing, the aim of this study is to analyze the nature and trends of LULCC over eastern South Africa and their impact on the local boundary layer climate during the satellite era from 1979 to 2020.

2. Data and methods

2.1. The study area

The study area is located southeast of South Africa on the Great Escarpment characterised by sharp topographic gradients that vary from 1040 to 2290 m above mean sea level, with lower altitudes in the east (figure 1). Rainfall and temperature vary quite significantly due to the complex topography.

LULCC is noticeable throughout the study area, and to provide a more detailed assessment, we divided the study area into four regions, identified as regions A, B, C, and D. Region A is Memel in Free State Province, dominated by agricultural activities (croplands) alongside a variety of other land cover types, including grassland and shrubs. Change in this region results largely from cropland expansion, which causes changes in other cover types. Region B is a developed urban area in the city of Newcastle, KwaZulu–Natal (KZN), surrounded by crops and shrubs. Due to population growth, this area has experienced an expansion of high-density urban settlements (townships), which have affected other land cover types, particularly crops. In region C is Normandien, KZN, which is distinguished by the Ntshingwayo Dam (previously Chelmsford), which consists of water bodies surrounded by crops and grassland. Water bodies in this area have changed over time and are likely influenced by nearby land use types such as cropland expansion, which necessitates water withdrawal. Region D in Paul Pietersburg, KZN, contains a variety of vegetation types, including crops, grasslands, and shrubs, but is primarily a eucalyptus forest, which experiences changes in forest harvesting/planting affecting crops and other land covers. The magnitude of these changes must be determined, and due to the diversity of LULC, it is an ideal location for this research, which will examine landscape change and determine the consequences of a changing climate.

2.2. Remote sensing data

When identifying and evaluating LULCC for the study, it is crucial to use imagery with no clouds or to remove clouds from the image. Cloud cover contaminates data and prevents efficient detection and extraction of required information from the image. However, due to limited satellite images with zero cloud cover, images with up to 10% cloud cover were also used in this study and treated as though they had no contamination (Mohajane *et al*. 2018). Landsat is well-known for its long-term earth observation records from orbit, and it has carried five generations of satellites since 1972 (Wulder *et al*. 2022). Landsat 5 (Thematic Mapper – TM), Landsat 7 (Enhanced Thematic Mapper Plus – ETM+), and Landsat 8 (Operational Land Imager – OLI) are used as secondary data sources. Our study sourced data from 1990 to 2020 for the LULCC analysis, accessed freely through the Google Earth Engine cloud platform. Landsat 5, 7, and 8 images were accessed according to the period of operation, and the 1T (first level) radiometric, geometric, and terrain-corrected images were used for image classification. Landsat images were chosen because of their high spatial resolution of 30 m × 30 m, which makes it ideal for LULC analysis (Li *et al*. 2011; Ding and Shi 2013), and they are widely used, and easily accessible (Ngie *et al*. 2014), with a 16-days revisit and can be used for long-term annual time series of land monitoring. Annual data allows for trend analysis over time, which is useful in determining the direction and magnitude of change. Land cover changes are gradual and may not be visible over short time spans, such as daily or monthly periods. Our study employed annual data to effectively capture and understand the cumulative impact of land cover dynamics on boundary layer climate to address this. The landsat-derived LST using mono-window and split-window algorithms was used as described by Sekertekin and Bonafoni (2020). Moreover, landsat-derived normalised deference vegetation index (NDVI) and normalised deference infrared index (NDII) were used as proxies for vegetation greenness and soil moisture storage, respectively. NDVI gauges spongy mesophyll (Gu *et al*. 2007) and is sensitive to chlorophyll levels (Burapapol and Nagasawa 2016), while NDII has proven to be a good indicator for monitoring root-zone soil moisture content based on the state of vegetation (Sriwongsitanon *et al*. 2015). LST, NDVI, and NDII have acquired prominence as indicators of drought conditions, surface soil moisture, and ET (Chikoore 2016). NDVI and NDII were computed with red, near-infrared (NIR), and shortwave infrared (SWIR) landsat spectral bands using equations (1 and 2), respectively.

$$NDVI = \frac{(NIR - Red)}{(NIR + Red)} \quad (1)$$

$$NDII = \frac{(NIR-SWIR)}{(NIR+SWIR)} \quad (2)$$

2.3. Climate data

The monthly Climate Hazards Group's Infrared Precipitation with Stations (CHIRPS) dataset was employed and accessed from the ClimateSERV website ClimateSERV – Map (servirglobal.net) to analyze rainfall variability. The CHIRPS dataset provides global data at daily, pentad, and monthly temporal resolution with a high spatial resolution of 0.05° × 0.05° (Funk *et al*. 2015). Furthermore, CHIRPS has a reasonably long record that spans the satellite era from 1981 to present, allowing for improved time series trend analysis for several environmental monitoring systems. This dataset provides dependable precipitation statistics, particularly in mountainous locations (Funk *et al*. 2015; Gebremicael *et al*. 2017; Shen *et al*. 2020). The CHIRPS data are primarily produced for agricultural drought monitoring (Funk *et al*. 2015), combining satellite (Meteosat) and station observations to provide the most accurate estimates of rainfall over complex terrains (Funk *et al*. 2015). CHIRPS data eliminates biases of satellite data, which often underestimate the severity of extreme rainfall events due to the complexity of the terrain and paucity of station data in most rural settings (Funk *et al*. 2015; Gebremicael *et al*. 2017).

The Global Land Data Assimilation System (GLDAS) version 1 data is a NOAH model, which is available from 1948 to 2000, and version 2 data is available from 2000 to present, with a spatial resolution of 0.25° × 0.25° and available monthly. GLDAS can generate quality-controlled, spatially, and temporally consistent data (Mbatha and Xulu 2018). Potential Evapotranspiration (PET) is a measure of atmospheric demand for water vapour and can be estimated using either the Thornthwaite or Penman–Monteith formulas, and the latter technique was used in this study. The Penman–Monteith technique combines fixed bulk surface and vapour aerodynamics to estimate PET (Tukimat *et al*. 2012) and is computed using daily mean temperature, wind velocity, humidity, and solar radiation or sunshine hours (Zhang *et al*. 2020). ET and PET data were downloaded from 1979 to 2020 from the Giovanni Earth Data website (https://giovanni.gsfc.nasa.gov/giovanni/). Sensible and latent heat fluxes constitute the transfer of heat between the land surface and the atmosphere due to differences in temperature and phase

changes of water (Ge *et al*. 2019). The heat flux data were also obtained from the GLDAS model, which was accessed from the Giovanni Earth Data website.

In this study, the Climate Research Unit gridded Time Series Version 4 (CRU TS v4) weather station observations at 2-m maximum (T_{max}) and minimum temperature (T_{min}) dataset were employed from 1979 to 2020 at 0.5° × 0.5° horizontal resolution and obtained via the KNMI climate explorer website: (http://climexp.knmi.nl/start.cgi). This monthly grid of land-based observations has no missing value and has been used for bias correction of the model and reanalyses, and the data is well described by Harris *et al*. (2020).

2.4. Methods

2.4.1. Classification algorithm

Supervised classification is a widely used technique that is entirely dependent on the researcher's knowledge of the area of study, which can be obtained through site visits, aerial images (Tarawally *et al*. 2018), or Google Earth's (GE) historical imaging function. Classification is the process of assigning spectral properties to individual pixels in an image to classify images as LULC classes (Lillesand *et al*. 2004; Mather and Koch 2011). The image is classified based on its spectral signature, and the training classes include the lowest and maximum features associated with each class's spectral signature. The landsat images were classified into different land cover classes using a machine learning Random Forest (RF) pixel-based supervised algorithm from 1990 to 2020, spanning 31 years of land usage. Breiman (2001) proposed the algorithm, which is based on decision trees, improved bagging, and the bootstrap technique. RF machine learning algorithm is used for object identification and classification as it has been shown in several studies (Kulkarni and Lowe 2016; Dlamini and Xulu 2019; Masroor *et al*. 2022) to be successful and produce high LULC accuracy results of more than 90%. It has become a popular algorithm since 2016 globally (Sheykhmousa *et al*. 2020) and one of the best techniques for distinguishing between urban and barren land (Masroor *et al*. 2022). The most important parameters in RF classifiers are the classification tree, the variable associated with each classification tree, the minimum sample size of leaves, and the decision tree input variables (Zhao *et al*. 2021). When the decision tree's accuracy is increased, the overall classification accuracy increases (Breiman 2001). The result of

supervised classification is highly dependent on the input training sample. A large sample set is required to train the classifier in complex domains to accurately discriminate between ground objects in complex topographic regions with diverse land cover and forest which may shadow areas and increase classification errors (Kulkarni and Lowe 2016). In this study, the initial categorization count began with 80 samples and gradually increased, and 70% of the sample was split for training and 30% for dataset validation. After each iteration, the classification results were compared to the corresponding satellite image, and if the classification results were not good, further training samples were added until a satisfactory classification result with an accuracy greater than 85% was attained. Xulu *et al*. (2021) effectively used RF to distinguish vegetation from non-vegetation areas in a South African mine area using GEE and reached a 78% accuracy. The classifier was also used in South Africa by Dlamini and Xulu (2019) during the classification of mining and forest classes at Richards Bay Minerals, achieving 99% accuracy. RF has been frequently used by researchers due to its decreased computational complexity and greater interpretability capacity (Sheykhmousa *et al*. 2020).

2.4.2. Accuracy assessment

All maps generated through remote sensing analysis must be validated against a comprehensive independent dataset (Hord and Brooner 1976; Xulu *et al*. 2021). Classification accuracy assessment is crucial (Mulugisi 2015) since without it, the classification is invalid (Odindi *et al*. 2017; Tarawally *et al*. 2018; Thapa 2020). Ground truthing was performed using GE to interpret land use. This study makes use of the historical imagery function to classify high-resolution GE images and validate the classified images. Two frequently used methods for assessing classification accuracy are the confusion/error matrix and kappa statistics. A confusion matrix is a component of standard descriptive and discrete multivariate statistics that are used to compare classification results to the actual data obtained (Mulugisi 2015). It is a technique used to summarise the performance of the classification algorithm (Lillesand *et al*. 2004) carried out by picking a representative sample of reference locations and comparing their classification to the classifications on the land cover map (Stehman 1997). The reference sample should be chosen independently of the data used to train and/or create the classification algorithm (Stehman 1997). A confusion matrix was generated to show the producer's accuracy (PA), the user's accuracy (UA), and the overall accuracy (OA). The kappa values are classified into three categories: Values <59%

indicate moderate or poor agreement, values between 60 and 79% indicate substantial agreement, and values >80% indicate strong agreement (Abdelkareem *et al*. 2018).

2.4.3. Time series analysis

Trend analysis is a statistical technique applied in this study to produce a temporal patterns of surface energy and moisture fluxes, and hydrometeorological parameters. Both parametric and nonparametric tests are routinely utilized to test the trend of time series data in climate, environmental, or hydrological data. The parametric test, according to Ahmad *et al*. (2015), requires normally distributed and independent data, whilst nonparametric tests require the data to be independent and resistant to outliers (Ahmad *et al*. 2015; Mbatha and Xulu 2018; Liu *et al*. 2021). When using a nonparametric test, results are not influenced by these outliers (Ahmad *et al*. 2015) or missing values (Liu *et al*. 2021). As a result, the nonparametric Mann–Kendall (MK) test was used to detect statistically significant time series trends in this study. The test uses the null hypothesis (H0), which argues that no trend exists, while the alternative hypothesis (H1) rejects the null hypothesis and states that a trend in parameters could be positive or negative (Ahmad *et al*. 2015). The trends were tested for statistical significance at the 95% level of confidence if *p*-values were <0.05.

2.4.4. Variable importance

Variable importance (VI) is used to rate or rank the importance of variables in regression or classification (Strobl *et al*. 2007; Debeer and Strobl 2020). Variables are presented in descending importance depicted by increased Mean Square Error (%IncMSE), which measures how much accuracy the model loses when a variable is altered, and the Increased Impurity Index (IncNodePurity), which measures how much each variable contributes to the homogeneity of the data in the resulting random forest (Echeverry-Galvis *et al*. 2014). The higher the value of %IncMSE or IncNodePurity, the higher the importance of the variable in the model. To determine the important hydrometeorological variable that influences climate variability, RF was employed using the 'random forest' library in R. An ensemble of classification trees was created in the RF by drawing several bootstrap samples or subsamples from the original training data and fitting a single classification tree to each sample (Strobl *et al*. 2008). As a result of random variation in the samples and the instability of the single classification trees, the ensemble in RF consists of a

diverse set of trees (Strobl *et al*. 2008; Debeer and Strobl 2020; Mathivha and Mbatha 2022). The RF is a model commonly used as a predictor function, and the model has been proven useful in a variety of applications (Debeer and Strobl 2020). It is popular and widely used due to its high prediction accuracy and ability to model high-dimensional complex data. In comparison to other univariable screening methods, RF can cover the impact of each predictor variable individually as well as in multivariate interaction with other predictor variables (Strobl *et al*. 2008). It was used in this study to rank the variables according to their importance, allowing for the identification of the most important or sensitive variable to change due to LULCC.

2.4.5. Multiple linear regression analysis

One of the study's objectives is to quantify the impact of different land uses/covers on critical variables that are sensitive to change in the local boundary layer climate and hence an MLR model was used. The MLR is a statistical technique that predicts the value of a single dependent variable using values of two or more independent variables (Alexopoulos 2010; Grant *et al*. 2019). It estimates the amount by which a dependent variable changes in response to changes in the independent variables (Grant *et al*. 2019). The MLR was used in this study to determine which land cover classes have the greatest influence on the important variable, allowing for the identification of the land cover class most likely to influence the local boundary layer climate. According to (Alexopoulos 2010; Mbatha and Xulu 2018), the MLR model can be represented as per equation (3).

$$y_i = \beta_0 + \beta_1 x_{i2} + \cdots \beta_p x_{ip} + \varepsilon_i \quad (3)$$

here $i = 1, 2, 3, \ldots, n$, y_i is the response variable which is the important variable as per random forest result, x_{ip} is the predictor's variables which are all classified LULC classes, β_0 is the intercept, and β_1, β_2, ... β_p is regression coefficient of the x terms. The term ε_i is the model's error terms, which it is always attempting to minimize (Mbatha & Xulu, 2018).

3. Results

3.1. Accuracy assessment

Several factors, including satellite data's properties, the scale of the research area, and the level of information in the LULC classes, can all have an impact on the accuracy value (Morales-Barquero *et al*. 2019). When identifying LULC using remote sensing, the total accuracy should be

at least 85%, and the classes should be at least 70% (Anderson 1976). Results show that the average overall classification accuracy and kappa coefficient ranged from 98 to 99% over the 31-year study period, indicating that classification accuracy is high. The validation data suggests that about 98% of the classification maps made in this study were highly accurate. This is a sufficient level of precision for subsequent analyses and change detection. The use of GEE and a RF classifier made it possible, and it has consistently demonstrated dependability.

3.2. Temporal and spatial analyses of land use land cover change

Landsat multispectral imagery from the GEE cloud platform was classified into six land cover categories annually for a period of 31 years (1990–2020) in the study area. The six categories, i.e., water, bare land, urban land, forest, cropland, and grassland, were classified based on their dominance in the area (figures 2 and 3). Figure 2 summarizes a time series of the LULCC through the study period, while figure 3 shows the spatial distribution of various LULC classes with 10-year intervals.

The MK trend test indicates a decreasing trend of water bodies in regions A and C ($p > 0.05$ and negative z value), while an increase is observed in regions B and D ($p > 0.05$ and positive z value; table 1). The variability in water bodies is much larger in region A than in the other regions. For example, the area covered by water bodies in 1997 and 2001 was above 300 and 400 ha, respectively, while in 2007 and 2020, the area was far <100 ha (figure 2a). This suggests that water bodies in regions A, B, and C are getting drier while those in region D are getting wetter, despite the trends being statistically insignificant. Cropland significantly decreased in regions A and B ($p <0.05$ and negative z value) while insignificantly decreasing and increasing in regions C and D, respectively (table 1).

Results also showed that grassland dominates all regions throughout the study period, covering more than 50% of the total area (figures 2 and 3). It has significantly decreased in regions B, C, and D while significantly increasing in region A (table 1). In regions A, B, and C, bare land is the second most dominant feature (figures 2a–c and 3a–c), whereas in region D, forest is the second dominant feature (figures 2d and 3d). In addition, the trend of bare land increased insignificantly in regions A, B, and D, while it significantly increased in region C ($p < 0.05$ and positive z value;

table 1). There is a clear relationship between grassland and bare land, with one decreasing as the other increases, and vice versa. A similar observation can be made between grassland and forest in region D (figure 2d). On the other hand, forest cover decreased significantly in region A but decreased insignificantly in region B and increased insignificantly in regions C and D (table 1). In region B, grassland significantly decreased from 1994 (61.4%) to 2014 (26.1%), then increased until 2020 (51%), whereas bare land experienced the opposite trend – an increase from 1994 (22.2%) to 2014 (52.8%) and a decrease from 2014 to 2020 (19.2%; figure 2b). In 2000, grassland showed a significant decrease and then recovered in 2001 in regions B and D (figure 2b and d), while region C only recovered in 2005 (figure 2c). Urban land increased significantly across all the regions (increased by 0.44% in region A, 15.5% in region B, 0.1% in region C, and 0.6% in region D) and was the only class that experienced significant, uninterrupted change as a result of human development and population growth over the 31-year period. As depicted in figures 2(b) and 3(b), region B demonstrates the greatest urban dominance and expansion. The expansion of urban land primarily occurs over both vegetated and bare land areas. Over regions A and C, urbanization expanded southwards at the expense of grassland (figure 3a and c), whereas region B expanded south and north over grassland and bare land (figure 3b), hence a significant decrease in the classes (figure 2b). While urban land expansion in region D is occurring on forested land and grassland, forest regeneration has occurred at the expense of grassland over time. This has provided clear evidence of deforestation as urbanization expands across region D.

3.3. Analysis of temporal and spatial distribution of climate variables

Latent heat flux (LHF), sensible heat flux (SHF), PET, T_{max} and rainfall values exhibit a distinct seasonality, with high values observed during the austral summer and low values in winter across all regions from 1979 to 2020 (figures 4–6). Over time, all the variables have undergone significant changes and fluctuations due to severe climatic conditions and extremes. The MK trend test revealed that all regions are characterized by an annual insignificant decreasing trend for LHF ($p >$ 0.05 and negative z value). The trend for SHF is significantly increasing ($p <$ 0.05 and positive z value) for regions B, C, and D, while increasing insignificantly in region A ($p >$ 0.05 and positive z value; table 2). The LHF and SHF are decreasing and increasing, respectively, at a faster rate in region D, with an LHF decrease of –0.243 W/m^2/year and a SHF increase of 0.252 W/m^2/year. Furthermore, in region A, the LHF decreased, and SHF increased at a slower rate, with

a decrease of –0.0316 W/m^2/year and an increase of 0.115 W/m^2/year, respectively. PET and T_{max} depicted a significant increasing trend ($p < 0.05$ and positive z value) in all regions (table 2). PET is trending similarly to SHF and in the opposite direction to LHF and ET (not shown), increasing west of the study area due to an increase in surface moisture deficits, which supports the temperature increase caused by a lack of evaporative surfaces (figures 4, 5(a–d), and 7). The atmospheric demand for moisture from the surface is high, so the area experienced a significant PET increase due to the increasing T_{max}. While PET increased in all regions, it is faster by 1.44 W/m^2/year in region B, while T_{max} is increasing faster by 0.0388°C/year in region C. High SHF and PET values are observed in region B (figures 4e–h and 5a–d), which can be attributed to impervious surface dominance and urban land expansion. This surface lacks moisture retention capacity, so high values can be observed.

Figure 5(e–h) shows that region B has high T_{max} annual average values ranging from 26° to 28°C, while region D has the lowest range of values ranging from 22° to 25°C. Figure 8 also supports this, showing that the eastern part of the study area has the highest average temperature while the western part has the lowest average temperature. This trend is similar to T_{min} (not shown). The coolest region, as shown by T_{min} and T_{max}, is characterized by an abundance of forest land in comparison to other regions, with high surface soil moisture observed in the forest but relatively dry over unforested LULC types. Soil moisture is utilized by plants during photosynthesis and supplied to the atmosphere as water vapour. Despite being characterized by low topography, region D still experienced low warming and increased surface soil moisture due to forest dominance compared to other regions. The overall result shows that both T_{min} and T_{max} have been increasing steadily since 1979, suggesting that the region is experiencing warming consistent with global trends. The increase in surface air temperatures is commensurate with increases in SHF and PET and a corresponding decrease in LHF, in agreement with Mbokodo *et al*. (2020). When temperatures rise, increased ET causes a water vapour shortage, threatening surface water resources.

Rainfall is the most important meteorological parameter in South Africa (Chikoore 2005), having significant impacts on the environment, human activities, and rural livelihoods. Table 2 shows that rainfall is characterized by a decreasing (not statistically significant) trend in regions B, C, and D

while increasing (not statistically significant) in region A. This suggests that regions B, C, and D are becoming drier over time, while region A is experiencing increasing rainfall of about 1.121 mm/year. Region D is drying faster at a rate of change of about –2.724 mm/year. Negative rainfall anomalies, which affected all regions during the summers of 1983/84, 1993/94, 2002/03, and 2015/16, suggest high vulnerability to dry spells and droughts. During these drought periods, SHF, PET, and T_{max} observed peaks while LHF and rainfall were low, with the 2015/16 El Niño season being the most extreme and intense (figures 4–6). Most importantly, all drought events affected the climate in region B the most in comparison to other regions due to the surface cover distributed across the area. However, during wet spells such as the 1984 tropical cyclones Domoina and Imboa, the 1996 tropical cyclone Bonita, and the 1998/99 La Niña phase, peaks of LHF and rainfall were observed, while SHF, PET, and T_{max} dropped (figures 4–6). During this period, region D experienced the most rainfall, recording more than 1100 mm of rainfall during the summer seasons of 1983/84, 1995/96, and 1998/99 (figure 6d), and this is the eastern part of the study that receives high rainfall (figure 8f–j).

Overall, results show that SHF has a positive relationship with PET and an inverse relationship with LHF (table 2, figures 4, 5a–d, and 7), which can be clearly seen during periods of dry and wet spells, where inverse fluctuations in both parameters are observed. Areas with forest cover have a higher LHF than areas with short or little vegetation (figure 4d and b). As such, LHF is observed spatially increasing eastward towards region D (figure 7a–e) as it is dominated by forests, higher than those of region B, characterised by urban centers. Areas with forests tend to experience low SHF (Ban-Weiss *et al*. 2011), as energy partitioning on vegetation cover favours LHF (Huang *et al*. 2020). Figure 5(d and h) also demonstrated that deep forest roots can supply the atmosphere's demand for moisture during periods of significant dry spells. Hence, the NDII result (not shown) exhibits significant high surface moisture over forest land and was less influenced by drought extremes.

3.4. Influence of land use and land cover change on the local boundary layer climate

3.4.1. Hydrometeorological variables, surface soil moisture, and energy flux sensitivity analysis

Figure 9 shows the variable of importance, which outlines the meteorological variables that are significant and have the most influence on temperature and rainfall. The variables are presented in descending importance from two qualitative measures produced by the model, which are the %IncMSE and the IncNodePurity. The higher the value of %IncMSE or IncNodePurity, the greater the importance of the variable in the model. The model shows in figure 9 that the variables that significantly influence temperature and rainfall are PET and LHF in all regions. However, the VI model also showed a different outcome, as rainfall in regions A and D was additionally significantly influenced by SHF, while region B was largely influenced by LST (figure 9e, f, and h). Changes in SHF affect atmospheric stability by modifying atmospheric radiative cooling and boundary layer height, resulting in the influence of rainfall processes (Ban-Weiss *et al*. 2011; Mahmood *et al*. 2014).

The VI showed that rainfall in regions A and D was influenced by both SHF and LHF, while in region B, it was influenced by both LHF and LST due to having two different variables with higher %IncMSE and IncNodePurity (figure 9). Therefore, correlation analysis of the variables of importance for rainfall and LHF, SHF, and LST (not shown) was performed to identify one with a significant correlation over regions A, B, and D. A significant correlation was found between rainfall and all the variables tested as depicted by p-value <0.05. Furthermore, Pearson R and p-values showed that a strong positive and significant correlation exists between rainfall and LHF in all the study regions. SHF and LST correlations with rainfall showed a significant but weak correlation, as shown by low Pearson R-values. This suggests that the increase in LHF influences rainfall more in comparison with SHF and LST in regions A, B, and D.

3.4.2. Climate sensitivity to LULCC

Table 3 shows a comprehensive summary of the MLR analysis statistics for six LULC classes using PET and LHF. This was carried out with PET and LHF as the most important variables that significantly influenced temperature and rainfall, respectively, as informed by VI analysis, and was thus used to attribute the impact of LULCC. Over the 31-year period, the MLR results revealed that the decrease in forests positively influenced temperature while also negatively influencing rainfall in region A. This suggests that the alteration of forest cover has increased surface temperatures and contributed to rainfall reduction in region A. Grassland in region B was found to

negatively influence rainfall as shown in table 3. The expansion of urban areas has positively influenced temperature in regions A, B, and D while negatively influencing rainfall in region B. The impact of urban growth is more pronounced in region B, as it has been associated with the reduction of rainfall. As shown in table 3, bare land had a positive influence on temperature in regions A, C, and D and a negative influence on rainfall in regions A and C. Cropland has a significant negative influence on rainfall in region C (table 3). Water bodies in regions B and C had a significant negative influence on temperature and a significant positive influence on rainfall in region D.

4. Discussion and conclusion

This study investigated the impact of LULCC on climate variability and the LULC classes that significantly affected the local boundary layer climate over eastern South Africa. From 1979 to 2020, changes in LULC classes were studied using a cloud-based RF classifier on the GEE platform. A critical step in the remote sensing satellite image classification process involves evaluating the accuracy of classification results. The accuracy of thematic maps constructed from multispectral imagery in this study was determined using an error or confusion matrix and basic descriptive statistics. The results clearly show that overall classification accuracy is satisfactory and correct, as it exceeds the 80% threshold for strong agreement, indicating that classification and actual ground classes agree. The MK trend test was used to detect the direction, magnitude, and statistical significance of trends of LULC, surface moisture and energy fluxes, and hydrometeorological variables. The VI identified the variables that are leading contributors to temperature and rainfall variability, whilst MLR identified the LULC class responsible for significant changes in climate. Overall, the LULC analysis revealed that there are significant changes in land surface characteristics in the study area. This is largely due to developmental activities and population growth, as urban areas have been subjected to enormous pressure, resulting in the conversion and transformation of cropland, grassland, water, forest, and bare land across all our study regions. Urban expansion is a major source of concern because it is irreversible and will have long-term impacts on the environment and climate, compared to vegetation fragmentation, which can be restored.

Results from the temporal and spatial analysis show variations and changes in surface soil moisture (not shown), energy fluxes, and hydrometeorological variables such as temperature, PET, and SHF due to LULCC and climate extremes. Overall, significant vegetation fragmentation and an increase in urban and bare land have contributed to surface moisture alteration leading to increased LST and SHF, whilst decreasing LHF in all the regions. SHF and LHF were sensitive to LULCC mainly due to changes in the albedo, evapotranspiration rate, and roughness length of the surface. The study also found that weather systems such as tropical cyclones and short-term rainfall variability can affect SHF and LHF, as evidenced by observed fluctuations during 1987/99, 1995/6, and 2006 wet spells, as well as during major drought events. When studied over shorter time periods, such as daily or monthly time scales, the short-term impact of energy fluxes due to short-term climate variability frequently outweighs the impact of LULCC. As a result, we focused on the impact of LULCC on an annual time scale, where the impacts become apparent and short-term weather events average out over longer periods.

LULCC alters the patterns of surface air temperature and rainfall (Mahmood *et al*. 2014). This study found that areas dominated by forests had higher precipitation and lower temperatures compared to their urban counterparts, which had reduced surface moisture and altered PET (increased), LHF (decreased), and SHF (increased). Rainfall and temperature changes show that the climate is changing over the area and will likely alter agriculture, food security, human health, and the economy (Chikoore 2005). The continuous change in LULC is likely to increase the occurrence and impacts of droughts, heatwaves, fire regimes, and floods (e.g., Mbokodo *et al*. 2020; Chikoore *et al*. 2021; Mashao *et al*. 2023; Mbokodo *et al*. 2023; Singo *et al*. 2023). Changes in temperature, rainfall, surface soil moisture, and energy fluxes can be attributed to LULCC, with the impact of the LULC class varying by latitude.

According to our MLR analysis, grassland and cropland negatively influenced rainfall in regions B and C, respectively, whereas forest fragmentation in region A has a positive influence on temperature but a negative impact on rainfall. It is well known that forest cover increases soil infiltration and storage capacity by absorbing excess rainwater and releasing it during dry periods (Abera *et al*. 2018). It aids in the capture of moisture to supply the atmosphere. Cropland, on the

other hand, has a greater evaporative cooling effect due to irrigation, which makes water accessible to the boundary layer climate (Boisier *et al*. 2012). As a result, cropland and forest fragmentation significantly impact the climate due to changes in surface roughness which directly enhance SHF during energy partitioning while decreasing low clouds associated with reduced evaporation (Ban-Weiss *et al*. 2011). We found that bare land positively influenced temperature in regions A, C, and D whilst negatively influencing rainfall in regions A and C, whereas urban land negatively influenced temperature in regions A, B, and D, as well as rainfall in region B. The urban area coverage in regions A and D is small compared to that in region B, but its importance to climate warming and variability was fundamental in this study. Zhou *et al*. (2016) reached a similar conclusion, indicating that while urban cover accounts for a small portion of global land cover, its impact on local, regional, and global warming is significant.

The impact of urban and bare land is mainly due to lower albedo, high heat absorption, and severe surface moisture deficits (Peña 2009; Tarawally *et al*. 2018; Meer and Mishra 2020). Regardless of the previous LULC type, urban land expansion warms the climate and decreases rainfall (Huang *et al*. 2020). This is because urban areas have a lower sky-view factor, less heat removal through wind, and the ability to store a significant amount of energy absorbed by walls and buildings (Mushore *et al*. 2018), all of which affect the local boundary layer climate. Furthermore, urban land can alter wind patterns, affecting the transport of moisture and heat and potentially disrupting the atmospheric circulation pattern. Moreover, water bodies negatively influenced temperature in regions B and C while having a positive influence on rainfall in region D. According to the study, local factors (lake breezes) in the vicinity of water bodies may have led to moderate temperatures while enhancing precipitation, regulating and reducing climate impact. This may be due to the fact that water bodies add moisture to the atmosphere, which aids in energy partitioning to favour LHF over SHF (Mushore *et al*. 2018), lowering temperatures and increasing cloud and rainfall formation (Meer and Mishra 2020). Thus, water bodies can be used to cool the climate during this vulnerable period and in urban settings, especially in the future, where climate extremes are expected to intensify (Mbokodo *et al*. 2020; IPCC 2021).

This study provides an important demonstration of LULCC and its influence on climate variability and change in South Africa. The study area's vulnerability to climate extremes will increase as the population grows in the future, resulting in more substantial LULCC. It demonstrates the importance of understanding the impact of LULCC on the climate to develop effective and appropriate plans and strategies for mitigating the impacts of climate change. We have provided some evidence to support understanding land–atmosphere interactions in a semi-arid climate and a region of complex topography, rapid population growth, and urban expansion.

Vegetation cover can be used to reduce the severity of heatwaves, droughts, and flooding by mitigating local warming, increasing precipitation, and reducing surface runoff (Abera *et al*. 2018). The impact of vegetation fragmentation and decline on climate in this study shows that it can be used as a mitigation strategy in this area. This necessitates more research and attention at different locations for resilience to climate change, as the impact of LULCC on the climate can be equivalent to, or even double or greater than, that of CO_2, and it varies per region (Mahmood *et al*. 2014). This necessitates prioritizing LULCC as a primary concern when assessing climate change, implying that more research is required.

The influence of short-lived boundary layer clouds on surface layer parameters is immediate and well-established. However, their impact on climate, which operates at vastly different timescales, remains comparatively unclear and is an active area of research. As a result, future studies need to address these limitations by modelling the impacts of cloud cover on the boundary layer climate and separating it from the impact of LULCC. This will further our understanding of the complex relationship between LULCC and boundary layer climate, which is very crucial in the climate system.

Overall, this study demonstrated that machine learning and the GEE platform are capable of mapping and analyzing large amounts of spatiotemporal data while producing high-quality and accurate results. The methodology used in this study can be expanded upon together with the use of climate models to better understand the dynamics of LULCC, boundary-layer climate, and

climate variability and change in South Africa. A physics-based climate model sensitivity study might reveal interesting insights, whilst the benefits of artificial intelligence can also be explored in future research. Future projections of LULCC in South Africa and its impacts on climate and the environment are critical, as is the influence of the future climate on the land surface. This will aid policy development by taking LULCC plans into account when addressing climate variability and change mitigation in South Africa.

Funding: This work was supported by the National Research Foundation and the North-West University of South Africa.

Acknowledgements: This work was originaly conceptualized from the MSc research of Tumelo Mohomi at the North-West Univerisity, South Africa. The data analyzed here were obtained from the Climate Research Unit of the University of East Anglia, University of Carlifornia, Santa Barbara, Natianal Aeronautics and Space Agency, and the United States Geological Survey.

Conflicts of interest: The authors declare no conflict of interest.

Author Statement

T.M. conceptualization, analyses, writing the original manuscript; N.B.M and D.S.B. supervision, revised and edited the manuscript; I.L.M., T.N. and M.M.B. edited the manuscript and provided comments; H.C conceptualization, supervision, edited the manuscript and provided comments.

References

Abdelkareem O E A, Elamin H M A, Eltahir M E S, Adam H E, Elhaja M E, Rahamtalla A M, ... and Elmar C 2018 Accuracy assessment of land use land cover in umabdalla natural reserved forest, South Kordofan, Sudan; *Int J Agric Environ Sci*. **3**(1) V-IX.

Abera T A, Heiskanen J, Pellikka P and Maeda E E 2018 Rainfall–vegetation interaction regulates temperature anomalies during extreme dry events in the Horn of Africa; *Global Planet. Change.* **167** XXXV-IV,. https://doi.org/10.1016/j.gloplacha.2018.05.002

Ahmad I, Tang D, Wang= T, Wang= M andWagan, B. 2015. Precipitation trends over time using Mann-Kendall and spearman's Rho tests in swat river basin, Pakistan; *Adv. Meteorol.* https://doi.org/10.1155/2015/431860

Ahmed B, Kamruzzaman M D, Zhu X, Shahinoor Rahman M D and Choi K 2013 Simulating land cover changes and their impacts on land surface temperature in dhaka, bangladesh, **5**(11) MMMMCMLXIX-(V)CMXCVIII; *Remote Sens*. https://doi.org/10.3390/rs5115969

Alexopoulos E C 2010 Introduction to multivariate regression analysis; *Hippokratia.* **14(Suppl 1)** XXIII.

Atayi J, Kabo-bah A T and Akpoti K 2016 The Effects of Large-Scale Mining on Land Use and Land Cover Changes Using Remotely Sensed Data; *Int. J. Sci. Nat.* **7** DCCXXIV-DCCXXXIII.

Ban-Weiss G A, Bala G, Cao L, Pongratz J and Caldeira K 2011 Climate forcing and response to idealized changes in surface latent and sensible heat; *Environ. Res. Lett.* **6**(3) XXXXMMMMXXXII. https://doi.org/10.1088/1748-9326/6/3/034032

Boisier J P, De Noblet-Ducoudré N, Pitman A J, Cruz F T, Delire C, Van Den Hurk B J J M, Van Der Molen M K, Mller C and Voldoire A 2012 Attributing the impacts of land-cover changes in temperate regions on surface temperature and heat fluxes to specific causes: Results from the first LUCID set of simulations; *J. Geophys. Res. Atmos.* **117**(D12). https://doi.org/10.1029/2011JD017106

Botha M, Siebert S J, Van den Berg J, Maliba B G and Ellis S M 2015 Plant and arthropod diversity patterns of maize agro-ecosystems in two grassy biomes of South Africa; *Biodiver. conserv*. **24**(7) MDCCXCVII-MDCCCXXIV.

Breiman L 2001 Random forests; *Machine Learning,* **45**(1) V-XXXII, https://doi.org/10.1023/A:1010933404324

Briassoulis H 2009 Factors Influencing Land-use and Land-Cover Change; In *Land Use, Land Cover and global change; EOLSS.* **1** pp CXXVI-CXLVI.

Burapapol K and Nagasawa R 2016 Mapping Soil Moisture as an Indicator of Wildfire Risk Using Landsat 8 Images in Sri Lanna National Park, Northern Thailand; *J. Agric. Sci,* **8**, CVII, https://doi.org/10.5539/jas.v8n10p107

Chikoore H 2005 Vegetation feedback on the boundary layer climate of southern Africa; *MSc dissertation, University of Zululand*

Chikoore H 2016 Drought in southern Africa: structure, characteristics and impacts; *PhD thesis, University of Zululand*

Chikoore H, Bopape M J M, Ndarana T, Muofhe T P, Gijben M, Munyai R B, Manyanya T C and Maisha R 2021 Synoptic structure of a sub-daily extreme precipitation and flood event in Thohoyandou, north-eastern South Africa; *Weather Clim. Extremes,* **33** CCCXXVII. https://doi.org/10.1016/j.wace.2021.100327

Chikoore H and Jury M R 2021 South African drought, deconstructed. *Weather Clim. Extremes,* **33** CXXXMMMCCCXXXIV. https://doi.org/10.1016/j.wace.2021.100334

Das S and Angadi D P 2020 Land use-land cover (LULC) transformation and its relation with land surface temperature changes: A case study of Barrackpore Subdivision, West Bengal, India; *Remote Sensing Applications: Soc. Environ,* **19** CXXXMMMCCCXXII. https://doi.org/10.1016/j.rsase.2020.100322

Debeer D and Strobl C 2020 Conditional permutation importance revisited; *BMC Bioinformatics.* **21**(1) I-XXX. https://doi.org/10.1186/s12859-020-03622-2

Ding H and Shi W 2013 Land-use/land-cover change and its influence on surface temperature: a case study

in Beijing City; *Int. J. Remote Sens.* **34**(15) VDIII–VDXVII. https://doi.org/10.1080/01431161.2013.792966

Dlamini L Z D and Xulu S 2019 Monitoring mining disturbance and restoration over RBM site in South Africa using landtrendr algorithm and landsat data; *Sustain. (Switzerland).* **11**(24) MCMXVI. https://doi.org/10.3390/SU11246916

Dong N, Liu Z, Luo M, Fang C and Lin H 2019 The Effects of Anthropogenic Land Use Changes on Climate in China Driven by Global Socioeconomic and Emission Scenarios; *Earth's Future,* **7**(7) DCCLXXXXIV-DCCCIV. https://doi.org/10.1029/2018EF000932

Echeverry-Galvis M A, Peterson J K and Sulo-Caceres R 2014 The social nestwork: Tree structure determines nest placement in Kenyan weaverbird colonies; *PLoS ONE,* **9**(2) e88761. https://doi.org/10.1371/journal.pone.0088761

Funk C, Peterson P, Landsfeld M, Pedreros D, Verdin J, Shukla S, Husak G, Rowland J, Harrison L, Hoell A and Michaelsen J 2015 The climate hazards infrared precipitation with stations - A new environmental record for monitoring extremes; *Sci. Data,* **2**(1), I-XXI, https://doi.org/10.1038/sdata.2015.66

Garg V, Nikam B R, Thakur P K, Aggarwal S P, Gupta P K and Srivastav S K 2019 Human-induced land use land cover change and its impact on hydrology; *HydroResearch,* **1** XLVIII-LVI, https://doi.org/10.1016/j.hydres.2019.06.001

Ge N, Zhong L, Ma Y, Cheng M, Wang X, Zou M and Huang Z 2019 Estimation of land surface heat fluxes based on landsat 7 ETM+ data and field measurements over the Northern Tibetan Plateau; *Remote Sens*. https://doi.org/10.3390/rs11242899

Gebremicael T, Mohamed Y, van der Zaag P, Berhe A, Haile G, Hagos E and Hagos M 2017 Comparison and validation of eight satellite rainfall products over the rugged topography of Tekeze-Atbara Basin at different spatial and temporal scales; *Hydrol. Earth Syst. Sci. Discuss,* I-XXXI , https://doi.org/10.5194/hess-2017-504

Grant S W, Hickey G L and Head S J 2019 Statistical primer: Multivariable regression considerations and pitfalls; *Eur. J. of Cardiothoracic. Surg,* **55**(2) CLXXIX-CLXXXV. https://doi.org/10.1093/ejcts/ezy403

Gu Y, Brown J F, Verdin J P and Wardlow B 2007 A five-year analysis of MODIS NDVI and NDWI for grassland drought assessment over the central Great Plains of the United States; *Geophys. Res. Lett.* **34**(6), https://doi.org/10.1029/2006GL029127

Güneralp B, Lwasa S, Masundire H, Parnell S and Seto K C 2018 Urbanization in Africa: Challenges and opportunities for conservation; *Environ. Res. Lett,* **13**(1) XVII. https://doi.org/10.1088/1748-9326/aa94fe

Gyamfi C, Ndambuki J M and Salim R W 2016 Hydrological responses to land use/cover changes in the Olifants Basin, South Africa. *Water (Switzerland).* https://doi.org/10.3390/w8120588

Harris I, Osborn T J, Jones P and Lister D 2020 Version 4 of the CRU TS monthly high-resolution gridded multivariate climate dataset; *Sci. Data,* **7**(1) I-XVIII. https://doi.org/10.1038/s41597-020-0453-3

Hord R M and Brooner W 1976 Land-use map accuracy criteria; *Photogrammetric Engineering and Remote Sens.* **42**(5) pp.671-7.

Herrmann S M, Brandt M, Rasmussen K and Fensholt R 2020 Accelerating land cover change in West Africa over four decades as population pressure increased; *Commun. Earth Environ.* **1**(1) I-1X, https://doi.org/10.1038/s43247-020-00053-y

Hu Xiaofang, Zhou W, Qian Y and Yu W 2017 Urban expansion and local land-cover change both significantly contribute to urban warming, but their relative importance changes over time; *Landsc Ecol*. **32**(4) DCCLXIII–DCCLXXXIX, https://doi.org/10.1007/s10980-016-0484-5

Huang Bo, Hu X, Fuglstad G A, Zhou X, Zhao W and Cherubini F 2020 Predominant regional biophysical cooling from recent land cover changes in Europe; *Nat. Commun.* **11**(1) I-XIII, https://doi.org/10.1038/s41467-020-14890-0

Idowu T E, Kiplangat N C and Waswa R 2019 Land cover changes and its Implications on Urban Heat Island in Nairobi County: A GIS and Remote Sensing Approach; *MKSU 2nd International Conference*, *April*, 16.

IPCC Climate Change 2021 The Physical Science Basis. Contribution of Working Group I to the Sixth Assessment Report of the Intergovernmental Panel on Climate Change; Masson-Delmotte V, Zhai P, Pirani A, Connors S, Péan C, Berger S, Caud N, Chen Y, Goldfarb L, Gomis M, et al., Eds.; Cambridge University Press: Cambridge, UK; New York, NY, USA, In press

Kamwi J M, Cho M A, Kaetsch C, Manda S O, Graz F P and Chirwa P W 2018 Assessing the spatial drivers of land use and land cover change in the protected and communal areas of the Zambezi Region, Namibia; *Land*. **7**(4), https://doi.org/10.3390/land7040131

Kulkarni A D and Lowe B 2016 Random Forest Algorithm for Land Cover Classification International Journal on Recent and Innovation Trends in Computing and Communication Random Forest Algorithm for Land Cover Classification; *Int. J. Recent Innov. Trends Comput Commun.*

Landman W A, Malherbe J and Engelbrecht F 2017 South Africa's present-day climate; In *S. Afri. Risk and Vulnerability Atlas*.

Li D, Tian P, Luo H, Hu T, Dong B, Cui Y, Khan S and Luo Y 2020 Impacts of land use and land cover changes on regional climate in the Lhasa River basin, Tibetan Plateau; *Sci. Total Environ.* **742** CXLMMDLXX, https://doi.org/10.1016/j.scitotenv.2020.140570

Li J, Song C, Cao L, Zhu F, Meng X and Wu J 2011 Impacts of landscape structure on surface urban heat islands: A case study of Shanghai, China; *Remote Sens. Environ*. **115**(12) MMMCCXLIX–MMMCCLXIII, https://doi.org/10.1016/j.rse.2011.07.008

Li X, Mitra C, Dong L and Yang Q 2018 Understanding land use change impacts on microclimate using Weather Research and Forecasting (WRF) model; *Physics and Chemistry of the Earth,* **103** CXV-CXXVI, https://doi.org/10.1016/j.pce.2017.01.017

Lillesand T M, Kiefer R W and Chipman J W 2004 Remote Sensing and Image Interpretation; In *John Wiley & Sons, New York, USA.*

Liu S, Bond-Lamberty B, Boysen L R, Ford J D, Fox A, Gallo K, Hatfield J, Henebry G M, Huntington T

G, Liu Z, Lovelan T R, Norby R J, Soh T, Steiner A L, Yuan W, Zhang Z and Zhao S 2017 Grand challenges in understanding the interplay of climate and land changes; *Earth Interact.* **21**(2) I-XLIII. https://doi.org/10.1175/EI-D-16-0012.1

Magidi J and Ahmed F 2020 Spatio-temporal variations of land surface temperature using Landsat and MODIS: case study of the City of Tshwane, South Africa; *S. Afr. J.l of Geomat,* **9**(2) CCCLXXIX-CCCXCVI

Mahmood R, Pielke R A, Hubbard K G, Niyogi D, Dirmeyer P A, Mcalpine C, Carleton A M, Hale R, Gameda S, Beltrán-Przekurat A, Baker B, Mcnider R, Legates D R, Shepherd M, Du J, Blanken P D, Frauenfeld O W, Nair U S and Fall S 2014 Land cover changes and their biogeophysical effects on climate; *Int. J. of Climatol.* **34**(4) CMXXIX-CMLIII, https://doi.org/10.1002/joc.3736

Masroor M, Avtar R, Sajjad H, Choudhari P, Kulimushi L C, Khedher K M, Komolafe A A, Yunus A P and Sahu N 2022 Assessing the Influence of Land Use/Land Cover Alteration on Climate Variability: An Analysis in the Aurangabad District of Maharashtra State, India; *Sustain. (Switzerland).* **14**(2), https://doi.org/10.3390/su14020642

Mather P M and Koch M 2011 Computer Processing of Remotely-Sensed Images; In *Computer Processing of Remotely-Sensed Images: an introduction. John Wiley & Sons.* https://doi.org/10.1002/9780470666517

Mathivha F and Mbatha N 2022 Comparison of Long-Term Changes in Non-Linear Aggregated Drought Index Calibrated by MERRA–2 and NDII Soil Moisture Proxies; *Water.* **14**(1) XXVI.

Mbatha N and Xulu S 2018 Time series analysis of MODIS-Derived NDVI for the Hluhluwe-Imfolozi Park, South Africa: Impact of recent intense drought; *Climate.* **6**(4) XCV, https://doi.org/10.3390/cli6040095

Mbithi D M, Demessie E T and Kashiri T 2006 The impact of Land Use Land Cover (LULC) changes on Land Surface Temperature (LST); a case study of Addis Ababa City , Ethiopia; *Kenya Metrological Services*, **1997** VIII.

Mbokodo I, Bopape M J, Chikoore H, Engelbrecht F and Nethengwe N 2020 Heatwaves in the future warmer climate of South Africa; *Atmosphere.* **11**(7) DCCXII, https://doi.org/10.3390/atmos11070712

Mbokodo IL, Bopape MJ, Ndarana T, Mbatha SM, Muofhe TP, Singo MV, Xulu NG, Mohomi T, Ayisi KK and Chikoore H 2023 Heatwave Variability and Structure in South Africa during Summer Drought; Climate. **11**(2) XXXVIII, https://doi.org/ 10.3390/cli11020038

Meer M S, and Mishra A K 2020 Land Use/Land Cover Changes over a District in Northern India using Remote Sensing and GIS and their Impact on Society and Environment; *J. Geol. Soc. of India.* **95**(2) CLXXIX-CLXXXII, https://doi.org/10.1007/s12594-020-1407-2

Morales-Barquero L, Lyons M B, Phinn S R and Roelfsema C M 2019 Trends in remote sensing accuracy assessment approaches in the context of natural resources; *Remote Sens*. **11**(19) MMCCCV, https://doi:10.3390/rs11192305

Mudau N, Mhangara P and Gebreslasie M 2014 Monitoring urban growth around Rustenburg, South Africa, using SPOT 5; *S. Afr. J.l of Geomat.* https://doi.org/10.4314/sajg.v3i2.5

Musetsho K D, Chitakira M and Nel W 2021 Mapping land-use/land-cover change in a critical biodiversity

area of south africa;. *Int. J. Environ Res. Public Health.* **18**(19) $\overline{X}\overline{C}\overline{L}\overline{X}\overline{I}\overline{V}$, https://doi.org/10.3390/ijerph181910164

Mushore Terence D, Mutanga O, Odindi J and Dube T 2018 Determining extreme heat vulnerability of Harare Metropolitan City using multispectral remote sensing and socio-economic data; *J. Spatial Sci.* **63**(1) CLXXIII-CXCI. https://doi.org/10.1080/14498596.2017.1290558

Namugize J N, Jewitt G and Graham M 2018 Effects of land use and land cover changes on water quality in the uMngeni river catchment, South Africa; *Phys. Chem. Earth, Parts a/b/c.* **105** CCXLVII-CCLXIV.

Ngie A 2020 Thermal remote sensing of urban climates in South Africa through mono-window algorithm; *Int. Arch Photogramm, Remote Sens. and Spatial Inf. Sci.* **43**(3/W11), https://doi.org/10.5194/isprs-archives-XLII-3-W11-117-2020

Ngie Adeline, Abutaleb K, Ahmed F, Darwish A and Ahmed M 2014 Assessment of urban heat island using satellite remotely sensed imagery: A review; *S. Afr. Geogr. J.* **96**(2) CXCVIII–CCXIV, https://doi.org/10.1080/03736245.2014.924864

Ngie A, Abutaleb K, Ahmed F, Taiwo O J, Darwish A A, and Ahmed M 2017 An estimation of land surface temperatures from landsat ETM+ images for Durban, South Africa; *Rwanda J.* https://doi.org/10.4314/rj.v1i2s.2d

Ngwana T I, Demory M E, Vidale P L, Plant R S and Mbedzi M P 2010 Impact of land cover changes on the South African climate; In IOP Conference Series: Earth and Environmental Science (Vol. 13, No. 1, p. 012009). IOP Publishing.

Nkosi M, Mathivha F I and Odiyo J O 2021 Impact of land management on water resources, a South African context; In *Sustainability (Switzerland)*. https://doi.org/10.3390/su13020701

Odindi J, Mhangara P and Kakembo V 2012 Remote sensing land-cover change in Port Elizabeth during South Africa's democratic transition; *S. Afri. J. Sci.* **108**(5) I-VII, https://doi.org/10.4102/sajs.v108i5/6.886

Odindi J, Mutanga O, Abdel-Rahman E M, Adam E and Bangamwabo V 2017 Determination of urban land-cover types and their implication on thermal characteristics in three South African coastal metropolitans using remotely sensed data; *S. Afr. Geogr. J.* **99**(1) LII-LXVII, https://doi.org/10.1080/03736245.2015.1117015

Ogwang B A, Ongoma V, Shilenje Z W, Ramotubei T S, Letuma M and Ngaina J N 2020 Influence of indian ocean dipole on rainfall variability and extremes over southern africa; *Mausam.* **71**(4) DCXXXVII-DCXLVIII.

Oki T and Blyth E 2012 Land cover and land use changes and their impacts on hydroclimate, ecosystems and society; In *Plenary Paper for the WCRP open science conference, Denver*.

Orimoloye I R, Ololade O O, Mazinyo S P, Kalumba A M, Ekundayo O Y, Busayo E T, Akinsanola A A and Nel W 2019 Spatial assessment of drought severity in Cape Town area, South Africa; *Heliyon,* **5**(7) e02148, https://doi.org/10.1016/j.heliyon.2019.e02148

Peña M A 2009 Examination of the land surface temperature response for santiago, Chile; *Photogramm. Eng. Remote Sens.* **75**(10) MCXCI-MCC, https://doi.org/10.14358/PERS.75.10.1191

Phan D C, Trung T H, Truong V T, Sasagawa T, Vu T P T, Bui D T, Hayashi M, Tadono T and Nasahara K N 2021 First comprehensive quantification of annual land use/cover from 1990 to 2020 across mainland Vietnam; *Sci. Rep.* **11**(1) I-XX, https://doi.org/10.1038/s41598-021-89034-5

Pielke R A, Pitman A, Niyogi D, Mahmood R, McAlpine C, Hossain F, Goldewijk K K, Nair U, Betts R, Fall S, Reichstein M, Kabat P and de Noblet N 2011 Land use/land cover changes and climate: Modeling analysis and observational evidence; *WIRES Climate Change.* **2**(6) DCCCXXVIII-DCCCL, https://doi.org/10.1002/wcc.144

Pontifes P A, García-Meneses P M, Gómez-Aíza L, Monterroso-Rivas A I and Caso-Chávez M 2018 Land use/land cover change and extreme climatic events in the arid and semi-arid ecoregions of Mexico; *Atmosfera*. **31**(4) CCCLV-CCCLXXII, https://doi.org/10.20937/ATM.2018.31.04.04

Rounsevell M D A, Arneth A, Alexander P, Brown D G, De Noblet-Ducoudré N, Ellis E, Finnigan J, Galvin K, Grigg N, Harman I, Lennox J, Magliocca N, Parker D, O'Neill B C, Verburg P H and Young O 2014 Towards decision-based global land use models for improved understanding of the Earth system; *Earth Syst. Dyn.* **5**(1) CXVII-CXXXVII, https://doi.org/10.5194/esd-5-117-2014

Sanecharoen W, Nakhapakorn K, Mutchimwong A, Jirakajohnkool S and Onchang R 2019 Assessment of urban heat island patterns in bangkok metropolitan area using time-series of LANDSAT thermal infrared data; *Environ. Nat. Resour. J.* **17**(4) LXXXVII-CII, https://doi.org/10.32526/ennrj.17.4.2019.34

Sazib N, Mladenova lliana E and Bolten J D 2020 Assessing the Impact of ENSO on Agriculture Over Africa Using Earth Observation Data; *Front. Sustain. Food Syst.* **4** 509914, https://doi.org/10.3389/fsufs.2020.509914

Sekertekin A and Bonafoni S 2020 Land surface temperature retrieval from Landsat 5, 7, and 8 over rural areas: Assessment of different retrieval algorithms and emissivity models and toolbox implementation; *Remote Sens.* **12**(2) CCXVCIC, https://doi.org/10.3390/rs12020294

Shen Z, Yong B, Gourley J J, Qi W, Lu D, Liu J, Ren L, Hong Y and Zhang J 2020 Recent global performance of the Climate Hazards group Infrared Precipitation (CHIRP) with Stations (CHIRPS); *J. Hydrol.* **591** 125284, https://doi.org/10.1016/j.jhydrol.2020.125284

Sheykhmousa M, Mahdianpari M, Ghanbari H, Mohammadimanesh F, Ghamisi P and Homayouni S 2020 Support Vector Machine Versus Random Forest for Remote Sensing Image Classification: A Meta-Analysis and Systematic Review; In *IEEE J. Sel. Top. Appl. Earth Obs. Remote Sens.* **13** VMCCCVIII-VMCCXXV, https://doi.org/10.1109/JSTARS.2020.3026724

Singleton A T and Reason C J C 2006 Numerical simulations of a severe rainfall event over the Eastern Cape coast of South Africa: Sensitivity to sea surface temperature and topography; *Tellus, Series A: Dyn. Meteorol. Oceanogr*. https://doi.org/10.1111/j.1600-0870.2006.00180.x

Solanky V, Singh S and Katiyar S K 2018 *Land Surface Temperature Estimation Using Remote Sensing Data*; (pp. CCCXLIII-CCCLI), https://doi.org/10.1007/978-981-10-5801-1_24

Sriwongsitanon N, Gao H, Savenije H H G, Maekan E, Saengsawang S and Thianpopirug S 2015 The Normalized Difference Infrared Index (NDII) as a proxy for soil moisture storage in hydrological modelling; *Hydrol. Earth Syst. Sci.s Discuss.* **12**(8), https://doi.org/10.5194/hessd-12-8419-2015

Stehman S V 1997 Selecting and interpreting measures of thematic classification accuracy; *Remote Sens. Environ.* **62**(1) LXXVII - LXXXIX, https://doi.org/10.1016/S0034-4257(97)00083-7

Strobl C, Boulesteix A L, Kneib T, Augustin T and Zeileis A 2008 Conditional variable importance for random forests; *BMC Bioinf.* **9**(1) I-II, https://doi.org/10.1186/1471-2105-9-307

Strobl C, Boulesteix A L, Zeileis A and Hothorn T 2007 Bias in random forest variable importance measures: Illustrations, sources and a solution; *BMC Bioinf.* **8**(1) I-XXI, https://doi.org/10.1186/1471-2105-8-25

Tarawally M, Xu W, Hou W and Mushore T D 2018 Comparative analysis of responses of land surface temperature to long-term land use/cover changes between a coastal and Inland City: A case of Freetown and Bo Town in Sierra Leone; *Remote Sens.* **10**(1) CXII. https://doi.org/10.3390/rs10010112

Thapa P 2020 Assessing the Impacts of Land Use and Land Cover Change on land surface temperature and precipitation : A case study in Kathmandu; *J. Geogr. Info. Syst.*

Tizora P, Le Roux A, Mans G and Cooper A 2016. Land use and land cover change in the Western Cape Province: quantification of changes & understanding of driving factors; *7 Th Planning Africa Conference 2016 - Making Sense of the Future: Disruption and Reinvention*.

Tukimat N N A, Harun S and Shahid S 2012 Comparison of different methods in estimating potential évapotranspiration at Muda Irrigation Scheme of Malaysia; *J. Agric. Rural Dev. Trop Subtrop (JARTS).* **113**(1) LXXVII-LXXXV.

Turok I and Borel-Saladin J 2014 Is urbanisation in South Africa on a sustainable trajectory?; *Dev South. Afr.* **31(5)** DCLXXV-DCLXXXXI, https://doi.org/10.1080/0376835X.2014.937524

Xulu S, Phungula P T, Mbatha N and Moyo I 2021 Multi-year mapping of disturbance and reclamation patterns over tronox's hillendale mine, south africa with dbest and google earth engine; *Land.* **10**(7) DCCLX. https://doi.org/10.3390/land10070760

Wulder M A, Roy D P, Radeloff V C, Loveland T R, Anderson M C, Johnson D M, ... and Cook, B. D. 2022 Fifty years of Landsat science and impacts; *Remote Sens. Environ*. **280** CXIIICXCV.

Yuvaraj R M 2020 Extents of Predictors for Land Surface Temperature Using Multiple Regression Model; *Sci. World J*. https://doi.org/10.1155/2020/3958589

Zhang C, Wang, X, Li J and Hua T 2020 Identifying the effect of climate change on desertification in northern China via trend analysis of potential evapotranspiration and precipitation; *Ecol. Indic.* **112** CVICXXXXMMMCXXXXI, https://doi.org/10.1016/j.ecolind.2020.106141

Zhou D, Li D, Sun G, Zhang L, Liu Y and Hao L 2016 Contrasting effects of urbanization and agriculture on surface temperature in eastern China; *J. Geophs. Res.* **121**(16) MMMMCXCVII - MMMMXDCVI, https://doi.org/10.1002/2016JD025359

TABLES

Table 1: Mann-Kendall trend test result (Z and p-value) and slope for the Land Use Land Cover classes

LULC	Region A			Region B			Region C			Region D		
	Z	*P*-value	Sen's Slope	Z	*P*-value	Sen's Slope	*Z*	*P*-value	Sen's Slope	Z	*P*-value	Sen's Slope
Water	-1.18	0.23	-1.67	-0.06	0.94	-0.14	-2.92	**0.003***	-15.2	0.61	0.54	1.61
Bare	0.48	0.63	27.3	1.69	**0.08**·	254.5	2.48	**0.01***	221.6	0.64	0.52	38.3
Urban	7.88	**3.11e-15*****	7.92	7.85	**4.08e-15*****	205.4	7.78	**7e-15*****	2.14	7.78	**7e-15*****	8.16
Forest	-2.88	**0.005*****	-6.22	-0.95	0.34	-4.74	0.06	0.94	1.50	2.99	**0.003*****	163.4
Cropland	-1.94	**0.05***	-8.79	-1.73	**0.08**·	-29.8	-0.61	0.46	0.54	-0.71	0.47	-3.34
Grassland	0.24	0.81	9.50	-4.08	**4.52e-05*****	-474.2	-1.97	**0.05***	-6.38	-4.35	**1.36e-05*****	-210.2

Significance codes: 0 '***' 0.001 '**' 0.01 '*' 0.05 '.' 0.1 ' ' 1.

Table 2: Mann-Kendall trend test result (Z and p-value) and slope for climate variables

Variable	Region A			Region B			Region C			Region D		
	Z	*P*-value	Sen's Slope	Z	*P*-value	Sen's Slope	Z	*P*-value	Sen's Slope	Z	*P*-value	Sen's Slope
LHF	-0.072	0.9421	-0.032	-1.427	0.154	-0.113	-1.427	0.1535	-0.166	-1.766	**0.077**·	-0.242
SHF	0.943	0.3454	0.115	2.056	**0.039** *	0.157	1.911	**0.0559** *	0.215	2.104	**0.035** *	0.251
PET	4.421	**9.8e-06*****	1.440	4.465	**8.0e-06*****	1.616	3.793	**0.0001*****	0.936	4.009	**6.1e-05*****	0.937
Tmax	4.421	**9.8e-06*****	0.038	4.519	**6.2e-06*****	0.038	4.400	**1.08-05*****	0.038	4.183	**2.8e-05*****	0.025
Rainfall	1.293	0.1959	1.121	-1.060	0.289	-1.449	-0.570	0.5681	-1.249	-0.454	0.649	-2.724

Significance codes: 0 '***' 0.001 '**' 0.01 '*' 0.05 '.' 0.1 ' ' 1.

Table 3: The output of Multiple Linear Regression (MLR) model over eastern South Africa with PET and LHF as a dependent variable and LULC classes as independent variables

LULC	Region A		Region B		Region C		Region D	
	PET	LHF	PET	LHF	PET	LHF	PET	LHF
Water	**-0.56*****	-0.52	**-0.0001*****	0.13	**-0.05**·	-0.11	0.42	**0.08**·
Bare Land	**2.54 x 10^{-06}*****	**-0.0002***	0.156	-0.93	**0.042** *	**-0.02** *	**0.02** *	-0.39
Urban	**3.70 x 10^{-11}** *	-0.13	**3.22 x 10^{-07}*****	**-0.039** *	0.189	0.38	**6.76 x 10^{-07}*****	-0.56
Forest	**0.044** *	**-0.03** *	-0.90	0.13	-0.94	0.99	-0.54	-0.32
Cropland	0.58	-0.27	0.11	-0.47	-0.16	**-0.028** *	0.604	-0.70
Grassland	NA	NA	0.23	**-0.05**·	NA	NA	NA	NA

Significance codes: 0 '***' 0.001 '**' 0.01 '*' 0.05 '.' 0.1 ' ' 1.

FIGURE CAPTIONS

Fig. 1(a): The eastern escarpment of South Africa is demarcated in a red rectangle on the highly vegetated eastern part of South Africa, and **Fig. 1**(b) this area encompasses three provinces namely KwaZulu Natal, Free State, and Mpumalanga. **Fig. 1**(c) The escarpment spans an altitude range of 580 to 2331 meters (m). **Fig. 1**(d) shows the location of four regions of interest, indicated by the maroon boxes, identified as insets A (Memel), B (Newcastle), C (Normandien), and D (Paulpieterburg).

Fig. 2: Long-term annual time series depicting variation of six (6) Land Use Land Cover classes from 1990 to 2020 at Region A (a), Region B (b), Region C (c), and Region D (d) over the eastern escarpment of South Africa.

Fig. 3: Temporal dynamic spatial mapping of land use and land cover (LULC) at Region A (a), Region B (b), Region C (c), and Region D (d) over the eastern escarpment of South Africa, based on 10-year interval spanning from 1990 to 2020.

Fig. 4: Long-term time series of monthly and annual latent heat flux (LHF; a-d) and sensible heat (SHF; e-h) for four regions (A-D) over the eastern escarpment of South Africa from 1979 to 2020.

Fig. 5: Long-term time series of monthly and annual potential evapotranspiration (PET; a-d) and the maximum temperature (Tmax, °C; e-h) for four regions (A_D) over the eastern escarpment of South Africa from 1979 to 2020.

Fig. 6: Long-term time series of monthly and annual rainfall in millimetres (mm) from 1981 to 2020 at Region A (a), Region B (b), Region C (c), and Region D (d) over the eastern escarpment of South Africa.

Fig. 7: Annual spatial variations of latent heat flux (LHF) for the years 1981 (a), 1990 (b), 2020 (c), 2010 (d), and 2020 (e); sensible heat flux (SHF) for the years 1981 (f), 1990 (g), 2020 (h), 2010 (i), and 2020 (j); and potential evapotranspiration (PET) during (k) 1981, (i) 1990, (m) 2020, (n) 2010, (o) 2020 over the eastern escarpment of South Africa. The black box denotes the four regions of interest.

Fig. 8: Annual spatial variations of maximum temperature (Tmax, °C) for the periods 1979 (a), 1990 (b), 2000 (c), 2010 (d), and 2020 (e); and rainfall during 1981 (f), 1990 (g), 2000 (h), 2010 (i) and 2020 (j) over the eastern escarpment of South Africa. The black box denotes the four regions of interest.

Fig. 9: Mean Decrease Accuracy (%IncMSE) and Mean Decrease Gini (IncNodePurity) of attributes as assigned by the Random Forest (RF) for maximum temperature (Tmax) at Region A (a), Region B (b), Region C (c), Region D (d); and rainfall at Region A (e), Region B (f), Region C (g), and Region D (h).

FIGURES

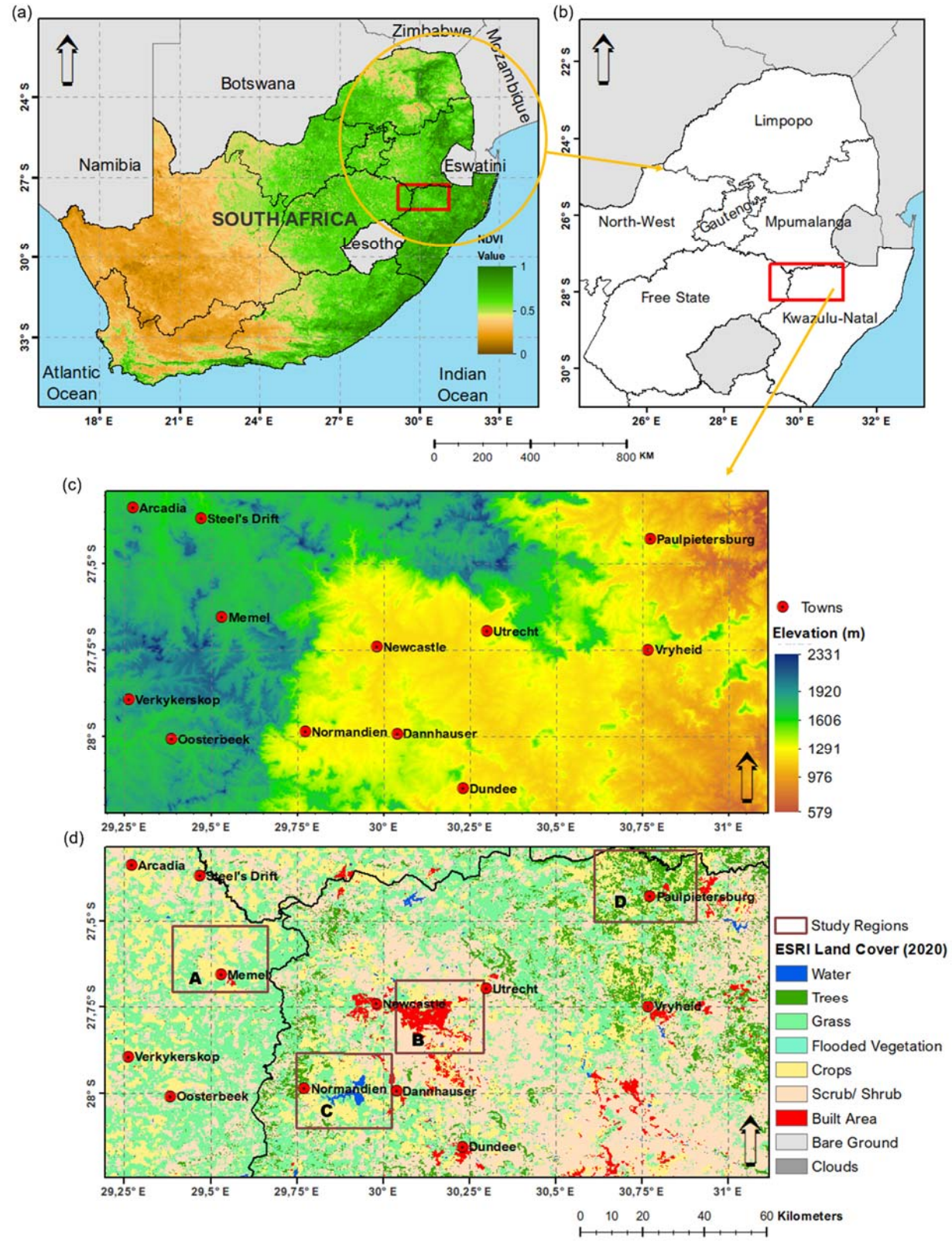

Fig. 1

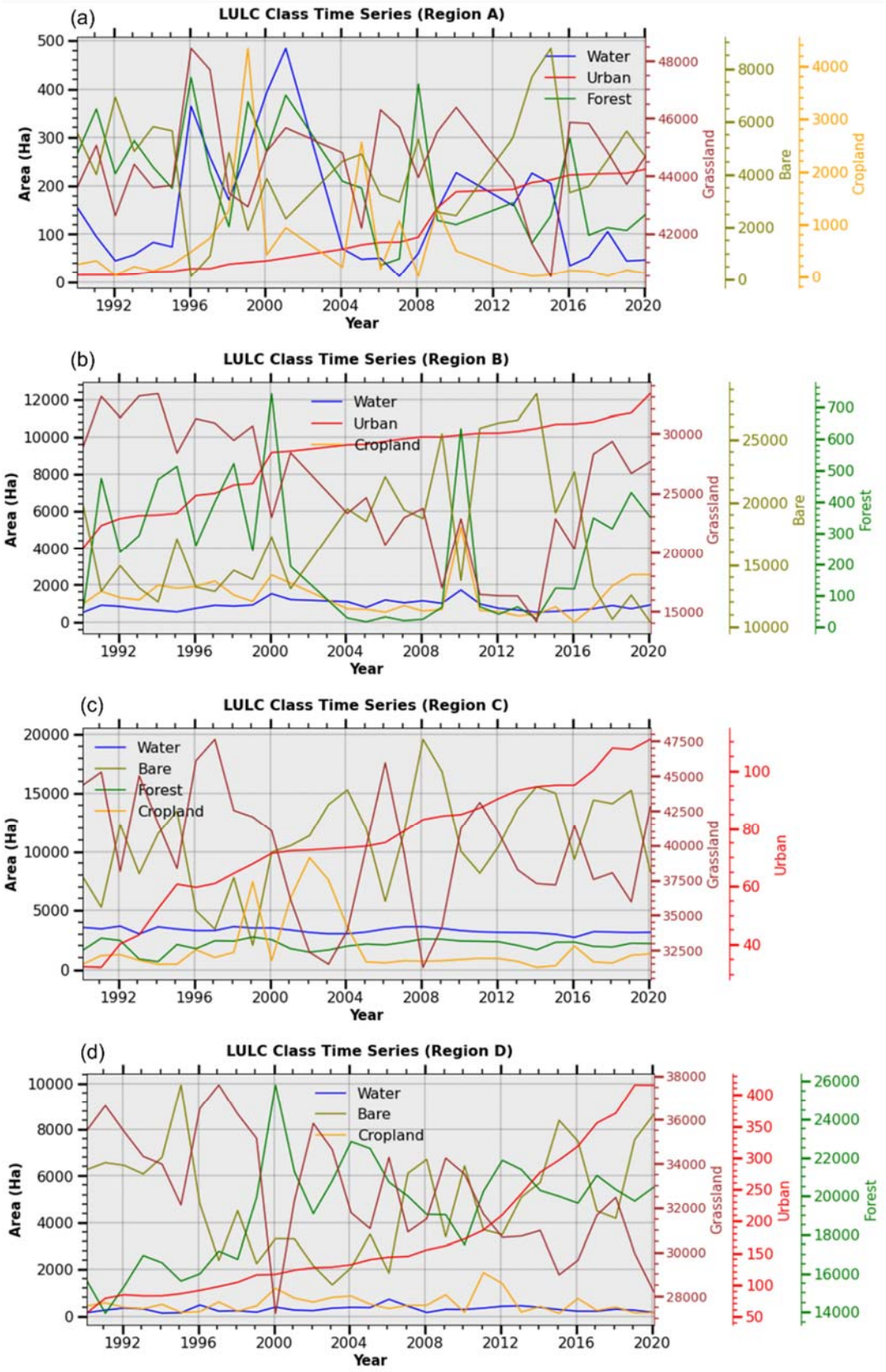
(a)
LULC Class Time Series (Region A)
Water
Urban
Forest
Area (Ha)
Grassland
Bare
Cropland
Year
(b)
LULC Class Time Series (Region B)
Water
Urban
Cropland
Area (Ha)
Grassland
Bare
Forest
Year
(c)
LULC Class Time Series (Region C)
Water
Bare
Forest
Cropland
Area (Ha)
Grassland
Urban
Year
(d)
LULC Class Time Series (Region D)
Water
Bare
Cropland
Area (Ha)
Grassland
Urban
Forest
Year

Fig. 2

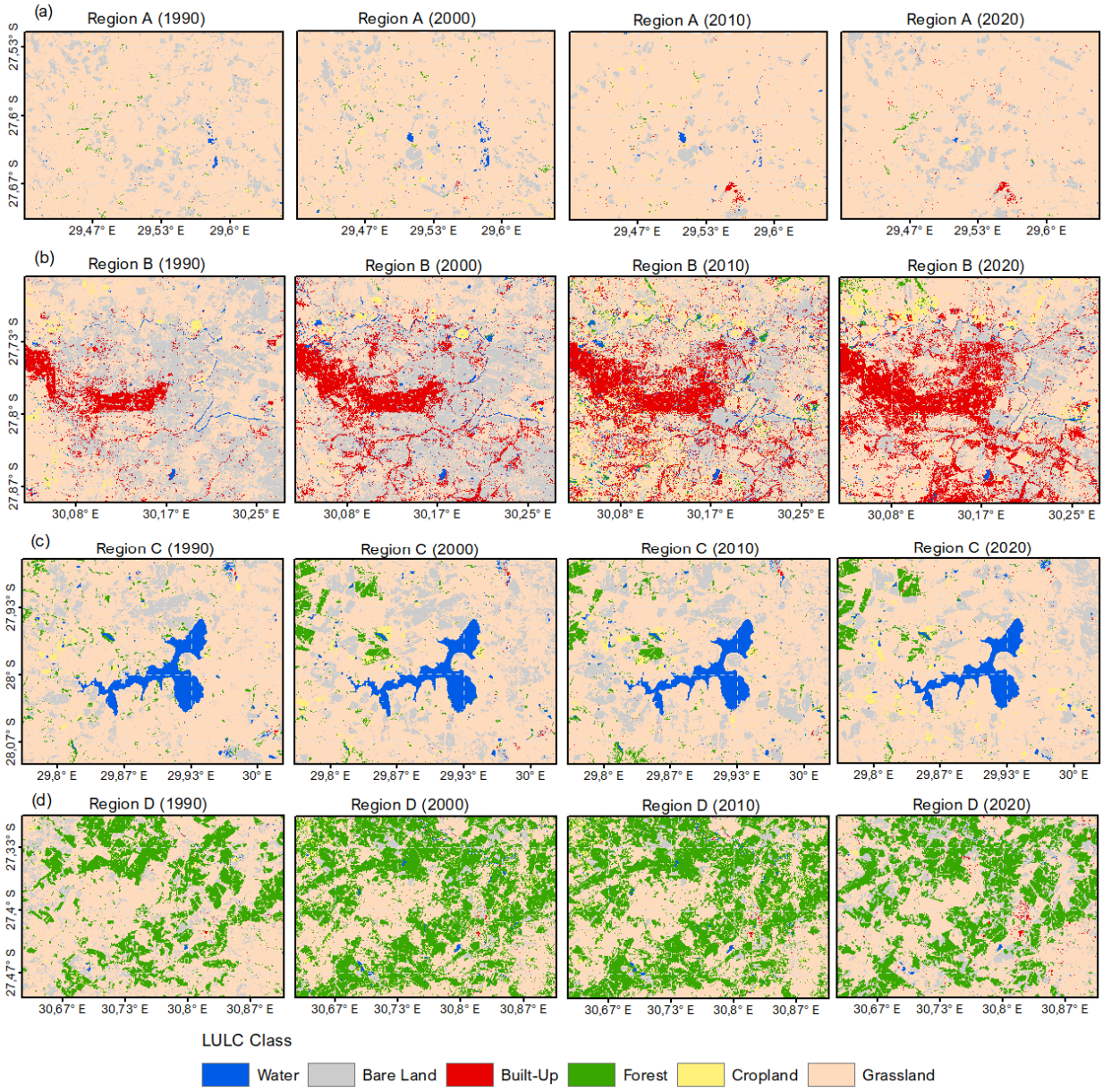
(a)
Region A (1990)
Region A (2000)
Region A (2010)
Region A (2020)
27,53° S
27,6° S
27,67° S
29,47° E
29,53° E
29,6° E
(b)
Region B (1990)
Region B (2000)
Region B (2010)
Region B (2020)
27,73° S
27,8° S
27,87° S
30,08° E
30,17° E
30,25° E
(c)
Region C (1990)
Region C (2000)
Region C (2010)
Region C (2020)
27,93° S
28° S
28,07° S
29,8° E
29,87° E
29,93° E
30° E
(d)
Region D (1990)
Region D (2000)
Region D (2010)
Region D (2020)
27,33° S
27,4° S
27,47° S
30,67° E
30,73° E
30,8° E
30,87° E
LULC Class
Water
Bare Land
Built-Up
Forest
Cropland
Grassland

Fig. 3

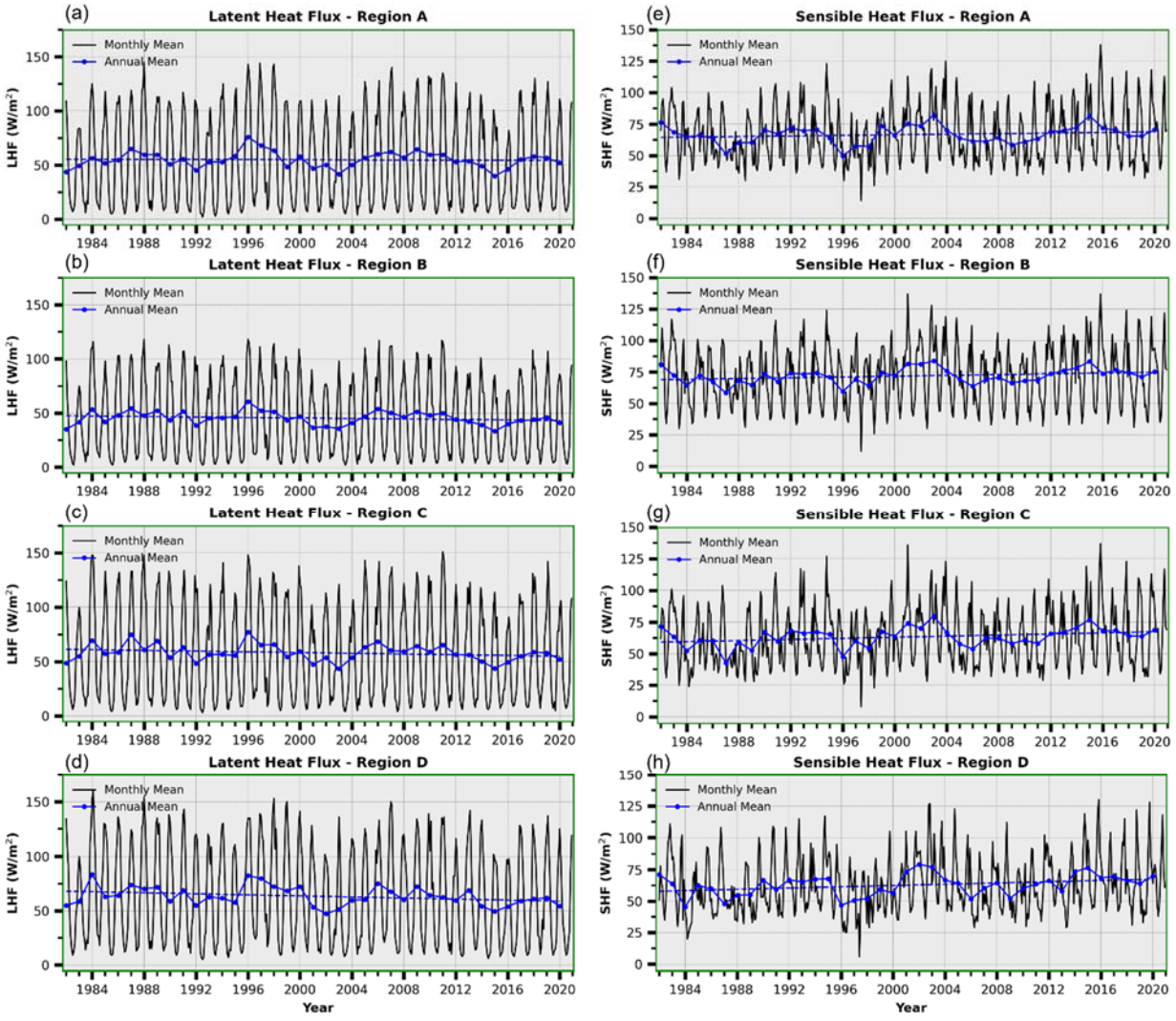
(a)
Latent Heat Flux - Region A
(b)
Latent Heat Flux - Region B
(c)
Latent Heat Flux - Region C
(d)
Latent Heat Flux - Region D
(e)
Sensible Heat Flux - Region A
(f)
Sensible Heat Flux - Region B
(g)
Sensible Heat Flux - Region C
(h)
Sensible Heat Flux - Region D
Monthly Mean
Annual Mean
LHF (W/m²)
SHF (W/m²)
Year

Fig. 4

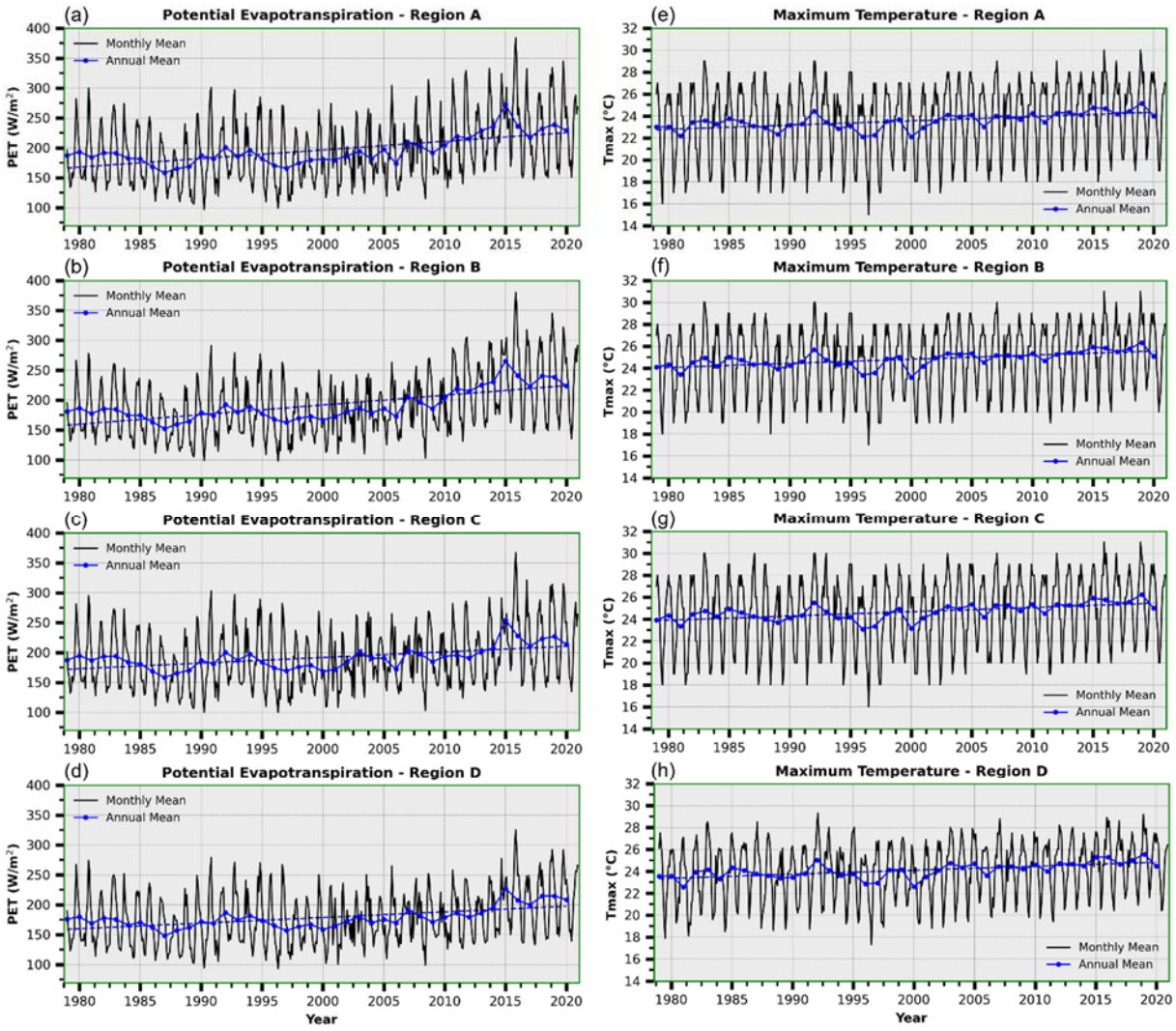
(a)
Potential Evapotranspiration - Region A
(b)
Potential Evapotranspiration - Region B
(c)
Potential Evapotranspiration - Region C
(d)
Potential Evapotranspiration - Region D
(e)
Maximum Temperature - Region A
(f)
Maximum Temperature - Region B
(g)
Maximum Temperature - Region C
(h)
Maximum Temperature - Region D
Monthly Mean
Annual Mean
PET (W/m²)
Tmax (°C)
Year

Fig. 5

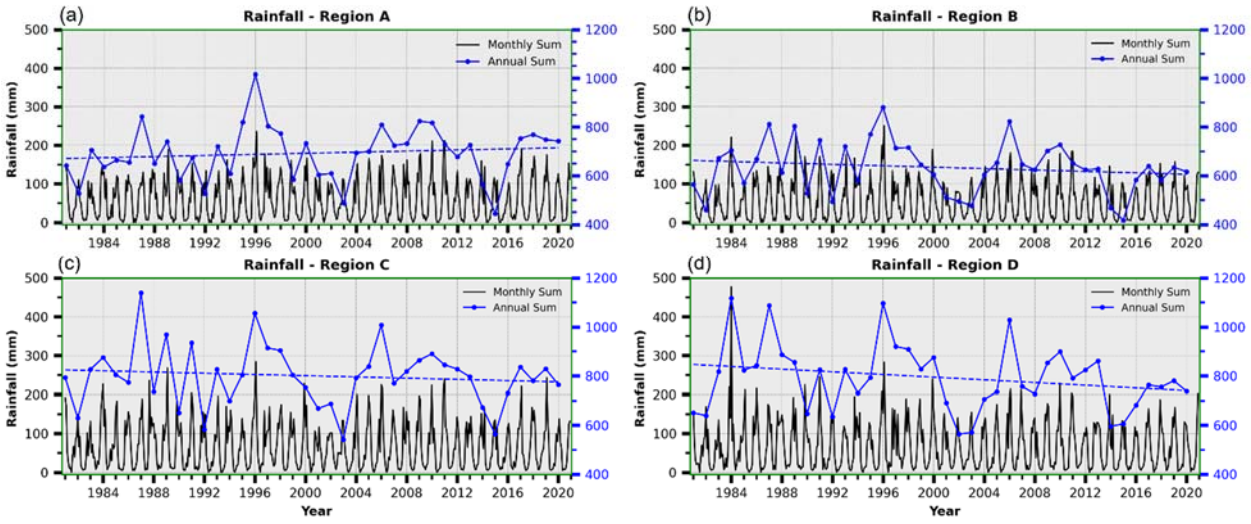
(a)
Rainfall - Region A
(b)
Rainfall - Region B
(c)
Rainfall - Region C
(d)
Rainfall - Region D
Monthly Sum
Annual Sum
Rainfall (mm)
Year
0
100
200
300
400
500
400
600
800
1000
1200
1984
1988
1992
1996
2000
2004
2008
2012
2016
2020

Fig. 6

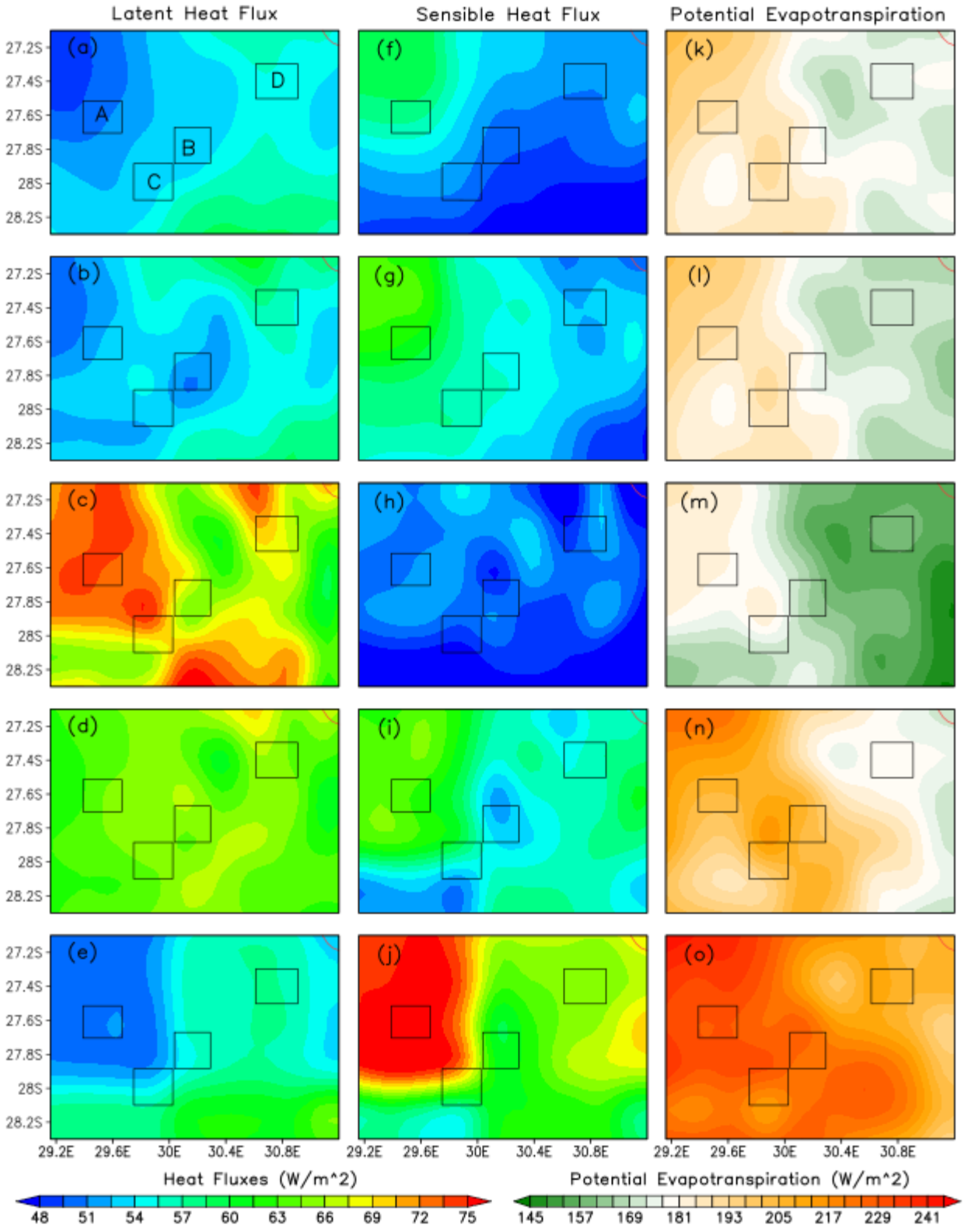
Latent Heat Flux
Sensible Heat Flux
Potential Evapotranspiration
(a)
(b)
(c)
(d)
(e)
(f)
(g)
(h)
(i)
(j)
(k)
(l)
(m)
(n)
(o)
A
B
C
D
27.2S
27.4S
27.6S
27.8S
28S
28.2S
29.2E
29.6E
30E
30.4E
30.8E
Heat Fluxes (W/m^2)
48 51 54 57 60 63 66 69 72 75
Potential Evapotranspiration (W/m^2)
145 157 169 181 193 205 217 229 241

Fig. 7

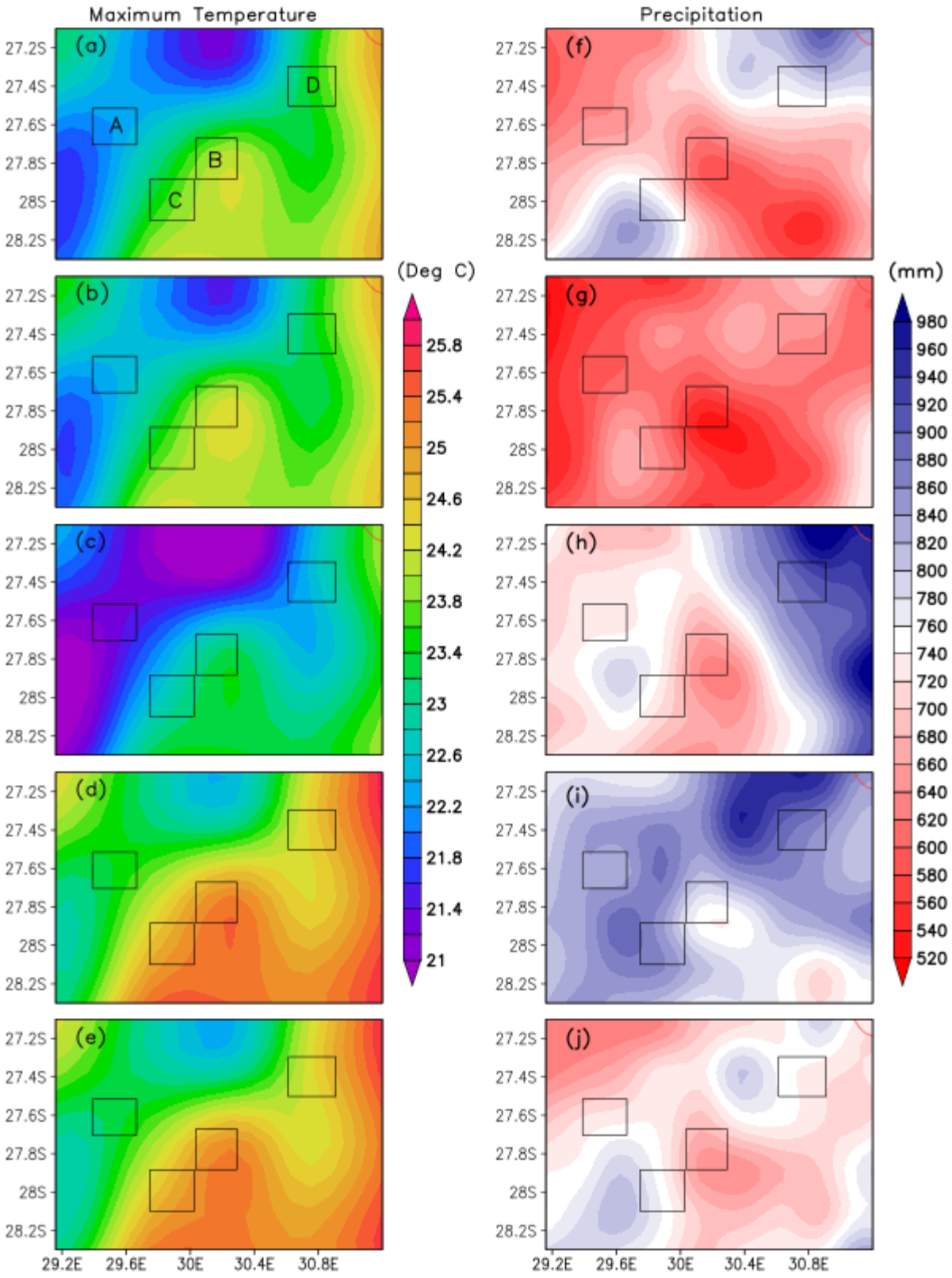
Maximum Temperature
Precipitation
(a)
(b)
(c)
(d)
(e)
(f)
(g)
(h)
(i)
(j)
A
B
C
D
(Deg C)
25.8
25.4
25
24.6
24.2
23.8
23.4
23
22.6
22.2
21.8
21.4
21
(mm)
980
960
940
920
900
880
860
840
820
800
780
760
740
720
700
680
660
640
620
600
580
560
540
520
27.2S
27.4S
27.6S
27.8S
28S
28.2S
29.2E
29.6E
30E
30.4E
30.8E

Fig. 8

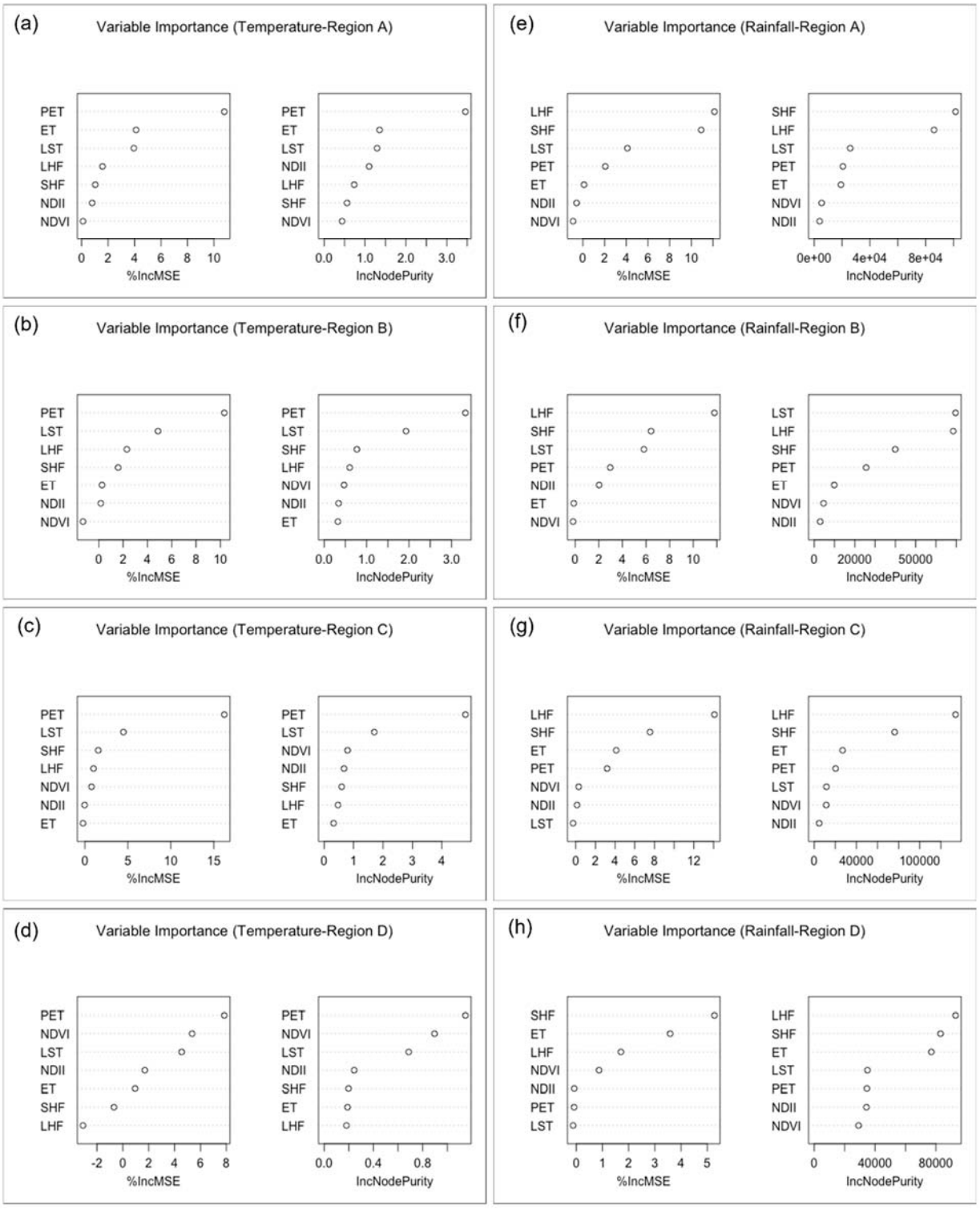
(a)
Variable Importance (Temperature-Region A)
PET
ET
LST
LHF
SHF
NDII
NDVI
0 2 4 6 8 10
%IncMSE
PET
ET
LST
NDII
LHF
SHF
NDVI
0.0 1.0 2.0 3.0
IncNodePurity
(e)
Variable Importance (Rainfall-Region A)
LHF
SHF
LST
PET
ET
NDII
NDVI
0 2 4 6 8 10
%IncMSE
SHF
LHF
LST
PET
ET
NDVI
NDII
0e+00 4e+04 8e+04
IncNodePurity
(b)
Variable Importance (Temperature-Region B)
PET
LST
LHF
SHF
ET
NDII
NDVI
0 2 4 6 8 10
%IncMSE
PET
LST
SHF
LHF
NDVI
NDII
ET
0.0 1.0 2.0 3.0
IncNodePurity
(f)
Variable Importance (Rainfall-Region B)
LHF
SHF
LST
PET
NDII
ET
NDVI
0 2 4 6 8 10
%IncMSE
LST
LHF
SHF
PET
ET
NDVI
NDII
0 20000 50000
IncNodePurity
(c)
Variable Importance (Temperature-Region C)
PET
LST
SHF
LHF
NDVI
NDII
ET
0 5 10 15
%IncMSE
PET
LST
NDVI
NDII
SHF
LHF
ET
0 1 2 3 4
IncNodePurity
(g)
Variable Importance (Rainfall-Region C)
LHF
SHF
ET
PET
NDVI
NDII
LST
0 2 4 6 8 12
%IncMSE
LHF
SHF
ET
PET
LST
NDVI
NDII
0 40000 100000
IncNodePurity
(d)
Variable Importance (Temperature-Region D)
PET
NDVI
LST
NDII
ET
SHF
LHF
-2 0 2 4 6 8
%IncMSE
PET
NDVI
LST
NDII
SHF
ET
LHF
0.0 0.4 0.8
IncNodePurity
(h)
Variable Importance (Rainfall-Region D)
SHF
ET
LHF
NDVI
NDII
PET
LST
0 1 2 3 4 5
%IncMSE
LHF
SHF
ET
LST
PET
NDII
NDVI
0 40000 80000
IncNodePurity

Fig. 9